PHYSICAL REVIEW B **93**, 125209 (2016)

Anisotropy, phonon modes, and free charge carrier parameters in monoclinic β-gallium oxide single crystals

M. Schubert,[1,2,*] R. Korlacki,[1] S. Knight,[1] T. Hofmann,[1,3] S. Schöche,[4] V. Darakchieva,[3] E. Janzén,[3] B. Monemar,[3,5] D. Gogova,[6,7] Q.-T. Thieu,[5,8] R. Togashi,[8] H. Murakami,[8] Y. Kumagai,[8] K. Goto,[8,9] A. Kuramata,[9] S. Yamakoshi,[9] and M. Higashiwaki[10]

[1]*Department of Electrical and Computer Engineering and Center for Nanohybrid Functional Materials, University of Nebraska, Lincoln, Nebraska 68588, USA*

[2]*Leibniz Institute for Polymer Research, Dresden, Germany*

[3]*Department of Physics, Chemistry, and Biology, IFM, Linköping University, SE-581 83 Linköping, Sweden*

[4]*J. A. Woollam Corporation, Inc.*

[5]*Global Innovation Research Organization, Tokyo University of Agriculture and Technology, Koganei, Tokyo, Japan*

[6]*Central Laboratory of Solar Energy and New Energy Sources, Bulgarian Academy of Sciences, Sofia, Bulgaria*

[7]*Leibniz Institute for Crystal Growth, Berlin, Germany*

[8]*Department of Applied Chemistry, Tokyo University of Agriculture and Technology, Koganei, Tokyo, Japan*

[9]*Tamura Corporation, Sayama, Saitama, Japan*

[10]*National Institute of Information and Communications Technology, Koganei, Tokyo, Japan*

(Received 28 December 2015; revised manuscript received 18 February 2016; published 15 March 2016)

We derive a dielectric function tensor model approach to render the optical response of monoclinic and triclinic symmetry materials with multiple uncoupled infrared and far-infrared active modes. We apply our model approach to monoclinic β-Ga_2O_3 single-crystal samples. Surfaces cut under different angles from a bulk crystal, (010) and $(\bar{2}01)$, are investigated by generalized spectroscopic ellipsometry within infrared and far-infrared spectral regions. We determine the frequency dependence of 4 independent β-Ga_2O_3 Cartesian dielectric function tensor elements by matching large sets of experimental data using a point-by-point data inversion approach. From matching our monoclinic model to the obtained 4 dielectric function tensor components, we determine all infrared and far-infrared active transverse optic phonon modes with A_u and B_u symmetry, and their eigenvectors within the monoclinic lattice. We find excellent agreement between our model results and results of density functional theory calculations. We derive and discuss the frequencies of longitudinal optical phonons in β-Ga_2O_3. We derive and report density and anisotropic mobility parameters of the free charge carriers within the tin-doped crystals. We discuss the occurrence of longitudinal phonon plasmon coupled modes in β-Ga_2O_3 and provide their frequencies and eigenvectors. We also discuss and present monoclinic dielectric constants for static electric fields and frequencies above the reststrahlen range, and we provide a generalization of the Lyddane-Sachs-Teller relation for monoclinic lattices with infrared and far-infrared active modes. We find that the generalized Lyddane-Sachs-Teller relation is fulfilled excellently for β-Ga_2O_3.

DOI: 10.1103/PhysRevB.93.125209

I. INTRODUCTION

Group-III sesquioxides have regained interest as wide band gap semiconductors with unexploited physical properties. Electric conductivity in transparent, polycrystalline, tin-doped In_2O_3 and Ga_2O_3 facilitates thin-film electrodes for smart windows [1,2], photovoltaics [1], large-area flat panel displays [3], and sensors, for example [4]. The highly anisotropic monoclinic β-gallia crystal structure (β phase) is the most stable crystal structure among the five phases (α,β,γ,ε, and δ) of Ga_2O_3 [5,6]. Mixed phase α-β Ga_2O_3 oxide junctions were recently discovered for high-activity photocatalytic water splitting [7]. Current research focusses on the development of single-crystalline group-III sesquioxide semiconductors with low defect densities for potential use as active materials in electronic and optoelectronic devices [8]. The thermodynamically stable β-Ga_2O_3 phase is of particular interest due to its large band gap energy of 4.85 eV, lending promise for applications in short-wavelength photonics and transparent electronics [9]. The high electric breakdown field value of β-Ga_2O_3, which is estimated at 8 MV cm^{-1}, exceeds those of contemporary semiconductor materials such as Si, GaAs, SiC, group-III nitrides, or ZnO [10]. Baliga's figure of merit for β-Ga_2O_3 is several times larger than those for 4*H*-SiC or GaN [11]. Baliga's figure of merit is the basic parameter to evaluate a material's suitability for power device applications. The figure of merit is proportional to the cube of the breakdown field, but only linearly proportional to mobility; hence, a large breakdown field can trump small mobility. Melt growth methods of bulk single crystals have been demonstrated by Czochralski growth [12], float zone growth [13], and edge-defined film-fed growth [14] suitable for mass production due to cost efficiency compared with growth of GaN substrates, for example [15]. Homoepitaxial thin film growth was developed by molecular beam epitaxy [10] and metal-organic vapor phase epitaxy methods [16], yielding good-quality crystalline materials. Schottky barrier diodes (SBDs) and metal-semiconductor field-effect transistors (MESFETs) on β-Ga_2O_3 homoepitaxial layers were reported for the first time by Sasaki *et al.* [10] and a breakdown voltage of 125 V was obtained. The MESFETs also exhibited excellent characteristics such as a nearly ideal

*schubert@engr.unl.edu; http://ellipsometry.unl.edu

pinch-off of the drain current, an off-state breakdown voltage over 250 V, a high on/off drain current ratio of around 10^4, and small gate leakage current [14]. These device characteristics clearly indicate the great potential of β-Ga_2O_3 as a high-power device material. It is also expected that extremely wide band gap semiconductors (with band gap energies larger than 4 eV) may have potential for so far unexplored optoelectronic applications in the deep-ultraviolet region. Such applications are emerging in the biotechnology and nanotechnology areas. For example, combining scanning near-field optical microscopy [17] with deep-ultraviolet transparent optical fibers [18] may enable imaging of molecular structures of DNA and proteins using characteristic absorption and/or fluorescence. Rare-earth or 3*d* transition metal doping in β-Ga_2O_3 thin films further demonstrated promising optical and photoluminescent properties, for example in thin-film electroluminescent devices [19,20].

Crucial for device design and operation is knowledge of electrical transport parameters. Likewise, understanding of heat transport as well as phonon-assisted free charge carrier scattering requires precise knowledge of long-wavelength phonon energies and band structure properties. In this paper we investigate lattice and free charge carrier properties of β-Ga_2O_3 by experiment and by calculation of phonon mode parameters. Knowledge of phonon modes and free charge carrier parameters is not exhaustive for β-Ga_2O_3. Very few reports exist on experimental determination of phonon mode parameters and their anisotropy [21]. No report exists to our best knowledge which observes and describes coupling of phonon and free charge carrier modes. Few reports exist on theoretical prediction and experimental determination of static and high-frequency dielectric constants and their anisotropy [22–28]. Calculations predict effective mass parameters [7,8,29–31], and few experiments were reported [32,33]. Theoretical descriptions of Brillouin zone center phonon modes are reported [28], and phonon band structures and density of states allowed prediction of thermal transport properties. Recently, Guo *et al.* measured the thermal conductivity in β-Ga_2O_3 single crystals and observed behaviors indicative of phonon-assisted heat transport with strongly anisotropic group velocities supported by first-principles calculations [34].

Owing to the unique strength of ellipsometry to resolve the state of polarization of light reflected off or transmitted through samples, both real and imaginary parts of the complex dielectric function can be determined at optical wavelengths [35–37]. Generalized ellipsometry extends this concept to arbitrarily anisotropic materials, and allows one to determine, in principle, all 9 complex-valued elements of the dielectric function tensor [38]. Jellison *et al.* reported generalized ellipsometry analysis of a monoclinic crystal, $CdWO_4$ [39]. Experimental data were taken from multiple sample orientations in the near-infrared to ultraviolet spectral regions. It was shown that 4 complex-valued dielectric tensor elements are required for each wavelength, which were determined spectroscopically, and independently of physical model line shape functions. The authors pointed out that no general rotations could be found to diagonalize the 4 tensor elements independently of wavelength. In the transparency region, a diagonalization could be found, but only one which depends on wavelength. Jellison *et al.* suggested to record and present, in general for monoclinic materials, 4 instead of 3 independent spectroscopic dielectric function tensor elements. In this context, a 4th spectroscopic response function is described, whose physical meaning, however, remained unexplained. Kuz'menko *et al.* and Möller *et al.* analyzed polarized reflectance from multiple surface orientations of monoclinic crystals, CuO and $MnWO_4$, respectively [40,41]. Spectra were obtained as a function of incident light polarization relative to the crystallographic axes. The authors used a physical function line shape model first described by Born and Huang [42]. This line shape model brings 4 interdependent dielectric function tensor elements into existence for monoclinic materials. Kuz'menko [43] described this model in more detail and exemplified analysis of the partially polarization-resolved reflectance spectra for monoclinic α-Bi_2O_3. The Born and Huang model allows for the derivation of TO modes and their unit eigendisplacement vectors. These were obtained and reported in Refs. [40,41,43]. However, numerical integrations were required to guarantee Kramers-Kronig consistency for the 4 tensor element spectra, since neither of these elements can be obtained independently and as complex-valued functions from reflectance data analysis. To our best knowledge, no independent verification of the Born and Huang model was provided for monoclinic crystals, where the dielectric tensor element functions have been determined independently and without physical line shape functions. Furthermore, the determination of longitudinal optical modes as well as plasma coupling in crystals with monoclinic symmetry has not been discussed and presented within the Born and Huang model. Also, the Lyddane-Sachs-Teller relation is not valid for monoclinic lattices and we present its generalization in this paper. We apply our model to β-Ga_2O_3 single crystals, and obtain and discuss fundamental physical parameters for this potentially important semiconductor material.

II. THEORY

The lattice constants of β-Ga_2O_3 are $a = 12.23$ Å, $b = 3.04$ Å, and $c = 5.80$ Å, and the monoclinic angle is $\beta = 103.7^\circ$ [44] (Fig. 2). There are ten atoms in the primitive unit cell of β-Ga_2O_3 with 30 normal modes of vibrations. The irreducible representations for acoustical and optical zone center modes are $\Gamma_{\text{aco}} = A_u + 2B_u$ and $\Gamma_{\text{opt}} = 10A_g + 4A_u + 5B_g + 8B_u$. For the optical modes, A_g and B_g modes are Raman active, while A_u and B_u modes are long-wavelength (infrared and far-infrared) active. Hence, β-Ga_2O_3 is a material with multiple modes of long-wavelength active phonons and plasmons. We provide a simple approach to construct the dielectric function tensor of materials with nonorthogonal normal modes. Born and Huang provided both an atomistic as well as a microscopic description of the lattice dynamics at long wavelengths from first principles and elasticity theory [42]. Both approaches lead to a description of the dielectric function tensor to which the result of our approach is equivalent. While our approach is straightforward, we extend the Born and Huang model by discussion of nonorthogonal longitudinal optical modes and coupling with plasma modes. All normal modes with transverse and longitudinal character predicted by theory are observed in our experiment and will be discussed in detail.

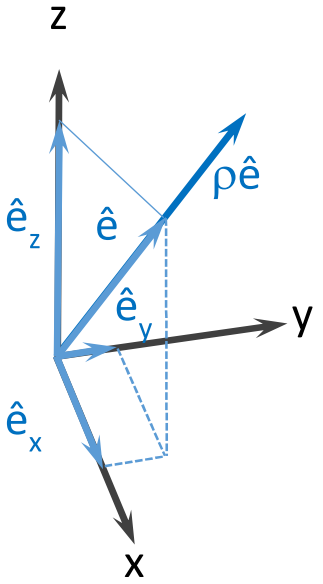

FIG. 1. Unit eigendisplacement vector $\hat{e}$ characteristic for a dielectric eigenpolarizability $\mathbf{P}_{\hat{e}}$ whose frequency response is rendered by a complex-valued response function $\varrho_{\hat{e}}$.

A. Uncoupled eigenpolarizability model

Intrinsic dielectric polarizations (eigendisplacement modes) of a homogeneous material give rise to long-wavelength active phonon modes. Each mode is associated with an electric dipole charge oscillation. The dipole axis can be associated with a characteristic eigenvector (unit eigendisplacement vector $\hat{e}$). Within the frequency domain, and within a Cartesian system with unit directions **x**, **y**, **z**, the dielectric polarizability **P** under the influence of an electric phasor field **E** along $\hat{\mathbf{e}} = \hat{e}_x\mathbf{x} + \hat{e}_y\mathbf{y} + \hat{e}_z\mathbf{z}$ is then given by a complex-valued response function $\varrho_{\hat{e}}$ (Fig. 1):

$$\mathbf{P}_{\hat{e}} = \varrho_{\hat{e}}(\hat{\mathbf{e}}\mathbf{E})\hat{\mathbf{e}}. \tag{1}$$

Function $\varrho_{\hat{e}}$ must satisfy causality and energy conservation requirements, i.e., the Kramers-Kronig integral relations and $\mathrm{Im}\{\varrho_{\hat{e}}\} \geqslant 0$, $\forall\,\omega \geqslant 0$ [45,46]. Under the assumption that different eigendisplacement modes do not couple, their eigenvectors may lie along certain, fixed spatial directions within a given sample of material. The linear polarization response of a material with m eigendisplacement modes is then obtained from summation:

$$\mathbf{P} = \sum_{l=1}^{m} \mathbf{P}_{\hat{e}_l} = \sum_{l=1}^{m} \varrho_{\hat{e}_l}(\hat{\mathbf{e}}_l \otimes \hat{\mathbf{e}}_l)\mathbf{E} = \chi\mathbf{E}, \tag{2}$$

where $\otimes$ is the dyadic product. Equation (2) results in a dielectric polarization response tensor χ, which is fully symmetric in all indices:

$$(\chi)_{ij} = \sum_{l=1}^{m} \varrho_{\hat{e}_l}\hat{e}_{i,l}\hat{e}_{j,l} = (\chi)_{ji}, i, j = \text{“}x\text{”},\text{“}y\text{”},\text{“}z\text{”}. \tag{3}$$

The mutual orientations of the eigenvectors and the frequency responses of their eigendisplacements determine the optical character of a given dielectrically polarizable material. For certain or all frequency regions, analogies can be found with symmetry properties of monoclinic, triclinic, orthorhombic, tetragonal, hexagonal, trigonal, or cubic crystal classes. The phasor field's displacement, **D**, and **E** are related by the dielectric function tensor (ε_0 is the vacuum permittivity):

$$\mathbf{D} = \varepsilon_0(1 + \chi\mathbf{E}) = \varepsilon_0\varepsilon\mathbf{E}. \tag{4}$$

Likewise to χ, ε is fully symmetric, invariant under time and space inversion, and a function of frequency ω. Chiral arrangements of eigendisplacements require augmentation of coupling between eigenmodes, which is not further discussed here. The dielectric function tensor in Eq. (4) has 6 independent complex-valued parameters. These render physical observables, which can be obtained by experiment, for example using generalized spectroscopic ellipsometry (GSE) [47]. The dielectric function tensor contains information on fundamental physical properties. For example, the frequencies of two characteristic optical modes, transverse optical (TO; ω_{TO}) and longitudinal optical (LO; ω_{LO}), can be obtained, respectively, from the roots of the determinants of ε^{-1}, and ε:

$$0 = \det\{\varepsilon^{-1}(\omega_{\mathrm{TO}})\}, \tag{5}$$
$$0 = \det\{\varepsilon(\omega_{\mathrm{LO}})\}. \tag{6}$$

Each of the modes ω_{TO} and ω_{LO} is associated with a unit eigendisplacement vector, $\hat{\mathbf{e}}_{\mathrm{TO}}$ and $\hat{\mathbf{e}}_{\mathrm{LO}}$, which can be obtained, respectively, from the set of equations

$$0 = \varepsilon^{-1}(\omega_{\mathrm{TO}})\hat{\mathbf{e}}_{\mathrm{TO}}, \tag{7}$$
$$0 = \varepsilon(\omega_{\mathrm{LO}})\hat{\mathbf{e}}_{\mathrm{LO}}. \tag{8}$$

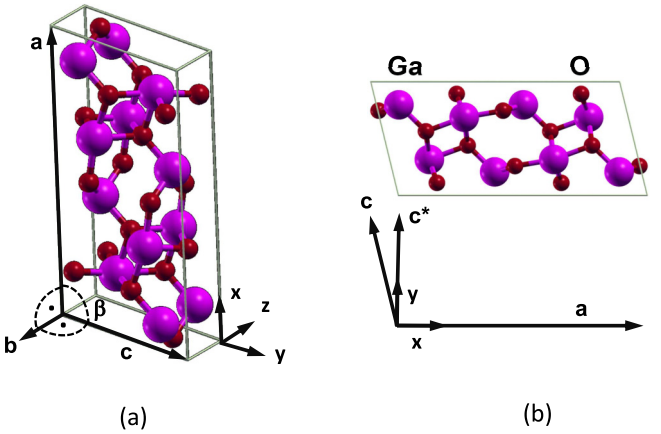

FIG. 2. (a) Unit cell of β-Ga_2O_3. Indicated are the monoclinic angle β and the Cartesian coordinate system (x, y, z) fixed to the unit cell in this work. (b) View onto the **a**-**c** plane along axis **b** which points into the plane. Indicated is the vector $\mathbf{c}^*$, defined for convenience here. See also Sec. IIC2 for further explanation.

B. Dielectric function tensor model for β-Ga_2O_3

Long-wavelength active phonon modes correspond to lattice displacements, which are associated with a linear dipole moment. In β-Ga_2O_3 (Fig. 2), 12 long-wavelength active phonon branches are predicted by symmetry. Each branch consists of a pair of TO and LO modes. In the presence of free charge carriers, 3 additional LO modes occur due to 3 available

dimensions for plasmon propagation. Their eigendisplacement vectors have to be determined from experiment, as will be discussed further below. The free charge carrier modes couple with the LO modes of the phonon branches unless their eigendisplacement vectors are orthogonal. This coupling leads to experimentally observable modes, the so called longitudinal phonon plasmon (LPP; ω_{LPP}) modes.

Transverse optical modes. Modes with A_u symmetry (4) are polarized along **b** only. Modes with B_u symmetry are polarized within the **a**-**c** plane. A choice of coordinates must be made at this step. We align unit cell axes **b** and **a** with $-\mathbf{z}$ and **x**, respectively, and **c** is within the (x-y) plane. We introduce vector $\mathbf{c}^\star$ parallel to **y** for convenience, and we obtain $\mathbf{a}, \mathbf{c}^\star, -\mathbf{b}$ as a pseudo-orthorhombic system (Fig. 2). Then, Eq. (2) leads to the following summations:

$$\mathbf{P}^{\beta-\mathrm{Ga_2O_3}} = \sum_{j=1}^{8} \varrho_j^{B_u} (\cos\alpha_j \mathbf{x} + \sin\alpha_j \mathbf{y}) + \sum_{k=1}^{4} \varrho_k^{A_u} \mathbf{z}, \quad (9)$$

where α_j describes the dipole oscillation axis of the jth B_u mode relative to **a**. As a result, and within the chosen coordinate frame, the dielectric function tensor has 4 independent complex-valued elements: $\varepsilon_{xx}, \varepsilon_{xy}, \varepsilon_{yy}$, and ε_{zz}.

The energy-dependent contribution to the long-wavelength polarization response of an uncoupled electric dipole charge oscillation is commonly described using a Lorentzian-broadened oscillator function [47,48]

$$\varrho_{(l)}(\omega) = \frac{A_{(l)}}{\omega_{\mathrm{TO},(l)}^2 - \omega^2 - i\omega\gamma_{(l)}}, \quad (10)$$

where $A_{(l)}$, $\omega_{\mathrm{TO},(l)}$, and $\gamma_{(l)}$ denote the amplitude, resonance frequency, and broadening parameter of a lattice resonance with TO character, ω is the frequency of the driving electromagnetic field, and $i^2 = -1$ is the imaginary unit. The index l numerates the contributions of all independent dipole oscillations.

Free charge carrier contributions. The energy-dependent contribution to the long-wavelength polarization response of free charge carriers is commonly described using the Drude model function [47,49–51]

$$\varrho_{\mathrm{FCC},(x,y,z)} = -\frac{e^2 N}{\tilde{\varepsilon}_0 m_{\mathrm{eff},(x,y,z)} \omega(\omega + i\gamma_{\mathrm{p},(x,y,z)})}, \quad (11)$$

where N is the free charge carrier volume density parameter. As discussed further below, we find the eigendisplacement vectors of the plasma modes orthogonal to each other, and we cast their contributions within the choice of Cartesian coordinates (x,y,z) shown in Fig. 2. Hence, the effective mass and plasma broadening parameters, $m_{\mathrm{eff},(x,y,z)}$ and $\gamma_{\mathrm{p},(x,y,z)}$, are indicated by their Cartesian axes, respectively ($\tilde{\varepsilon}_0$ is the vacuum permittivity, and e is the amount of the electrical unit charge). The plasmon broadening parameters can be related to optical mobility parameters $\mu_{(x,y,z)}$:

$$\gamma_{\mathrm{p},(x,y,z)} = \frac{e}{m_{\mathrm{eff},(x,y,z)} \mu_{(x,y,z)}}. \quad (12)$$

High-frequency dielectric constants. Equations (10) and (11) vanish for large frequencies; however, contributions to the polarization functions may arise from higher frequency charge oscillations such as electronic band-to-band transitions. A full analysis requires the incorporation of experimental data far into the ultraviolet region to identify the eigendisplacement vectors of the electronic band-to-band transitions in β-Ga_2O_3. Because the fundamental band-to-band transition energy is far outside the spectral range investigated here, we approximate the high-frequency contributions by frequency-independent parameters which represent the sum of all contributions from all higher-energy electronic band-to-band transitions:

$$\boldsymbol{\varepsilon}_\infty = \begin{pmatrix} \varepsilon_{\infty,xx} & \varepsilon_{\infty,xy} & 0 \\ \varepsilon_{\infty,xy} & \varepsilon_{\infty,yy} & 0 \\ 0 & 0 & \varepsilon_{\infty,zz} \end{pmatrix}. \quad (13)$$

Note that due to the monoclinic symmetry, 4 real-valued parameters are required. An effective eigendisplacement vector can be found from Eq. (3) for the band gap spectral region, which may also be considered as effective monoclinic angle for this spectral region:

$$\alpha_\infty = \tan^{-1}\left(\frac{\varepsilon_{\infty,xy}}{\varepsilon_{\infty,xx} - 1}\right) = \cot^{-1}\left(\frac{\varepsilon_{\infty,yy} - 1}{\varepsilon_{\infty,xy}}\right). \quad (14)$$

Static dielectric constants. Equation (10) contributes constant values at zero frequencies, when free charge carrier contributions in Eq. (11) are absent:

$$\boldsymbol{\varepsilon}_{\mathrm{DC}} = \begin{pmatrix} \varepsilon_{\mathrm{DC},xx} & \varepsilon_{\mathrm{DC},xy} & 0 \\ \varepsilon_{\mathrm{DC},xy} & \varepsilon_{\mathrm{DC},yy} & 0 \\ 0 & 0 & \varepsilon_{\mathrm{DC},zz} \end{pmatrix}. \quad (15)$$

The contributions are obtained explicitly as

$$\varepsilon_{\mathrm{DC},xx} = \varepsilon_{\infty,xx} + \sum_{j=1}^{8} \cos^2\alpha_j \frac{A_j^{B_u}}{\omega_{\mathrm{TO},j}^2}, \quad (16)$$

$$\varepsilon_{\mathrm{DC},xy} = \varepsilon_{\infty,xy} + \sum_{j=1}^{8} \sin\alpha_j \cos\alpha_j \frac{A_j^{B_u}}{\omega_{\mathrm{TO},j}^2}, \quad (17)$$

$$\varepsilon_{\mathrm{DC},yy} = \varepsilon_{\infty,yy} + \sum_{j=1}^{8} \sin^2\alpha_j \frac{A_j^{B_u}}{\omega_{\mathrm{TO},j}^2}, \quad (18)$$

$$\varepsilon_{\mathrm{DC},zz} = \varepsilon_{\infty,zz} + \sum_{k=1}^{4} \frac{A_k^{A_u}}{\omega_{\mathrm{TO},k}^2}. \quad (19)$$

Hence, 4 constitutive parameters may be required near DC frequencies to describe the dielectric response of β-Ga_2O_3. An effective monoclinic eigendisplacement vector within the **a**-**c** plane can be found from Eq. (3), valid near DC frequencies only:

$$\alpha_{\mathrm{DC}} = \tan^{-1}\left(\frac{\varepsilon_{\mathrm{DC},xy}}{\varepsilon_{\mathrm{DC},xx} - 1}\right) = \cot^{-1}\left(\frac{\varepsilon_{\mathrm{DC},yy} - 1}{\varepsilon_{\mathrm{DC},xy}}\right). \quad (20)$$

Dielectric function tensor. The β-Ga_2O_3 monoclinic dielectric function tensor is composed of the high-frequency contributions, the dipole charge resonances, and the free charge

carrier contributions:

$$\varepsilon_{xx} = \varepsilon_{\infty,xx} + \sum_{j=1}^{8} \varrho_j^{B_u} \cos^2 \alpha_j + \varrho_{\mathrm{FCC},x}, \tag{21a}$$

$$\varepsilon_{xy} = \varepsilon_{\infty,xy} + \sum_{j=1}^{8} \varrho_j^{B_u} \sin \alpha_j \cos \alpha_j, \tag{21b}$$

$$\varepsilon_{yy} = \varepsilon_{\infty,yy} + \sum_{j=1}^{8} \varrho_j^{B_u} \sin^2 \alpha_j + \varrho_{\mathrm{FCC},y}, \tag{21c}$$

$$\varepsilon_{zz} = \varepsilon_{\infty,zz} + \sum_{k=1}^{4} \varrho_k^{A_u} + \varrho_{\mathrm{FCC},z}, \tag{21d}$$

$$\varepsilon_{xz} = \varepsilon_{zx} = 0. \tag{21e}$$

Equations (21) provide valuable insight into the dielectric function tensor elements. If modes with A_u and B_u symmetry are distinct, critical point features [52] due to responses at frequencies with A_u symmetry should only occur in ε_{zz}. Features due to modes with B_u symmetry should only occur in ε_{xx},ε_{xy}, and ε_{yy}. Depending on the orientation of the unit eigendisplacement vector of a given mode, contributions may occur either (i) in ε_{xx} ($\alpha = 0°$) only, (ii) in ε_{yy} ($\alpha = 90°$) only, or (iii) in all ε_{xx},ε_{xy}, and ε_{yy} ($\alpha \neq n\pi, n = 0, \pm 1, \pm 2, \ldots$). Element ε_{xy} is different from zero in case (iii) only. The imaginary part of ε_{xy} can be negative. The latter provides a unique experimental access to identify whether α for a given mode shares an acute, a right, or an obtuse angle with the **a** axis. Note that ε_{xx},ε_{xy}, and ε_{yy} overdetermine the intrinsic polarizability functions. This is because ε_{xy} is the product of simple geometrical shear projections and not the result of new or additional physical properties in materials with nonorthogonal unit eigendisplacement vectors of intrinsic modes.

LO mode determination. The determinant in Eq. (6) factorizes into 2 equations, one valid for electric field polarization within the x-y plane, and one equation valid for polarization along z, respectively:

$$0 = \varepsilon_{xx}\left(\omega_{\mathrm{LO}_{(n)}}\right)\varepsilon_{yy}\left(\omega_{\mathrm{LO}_{(n)}}\right) - \varepsilon_{xy}^2\left(\omega_{\mathrm{LO}_{(n)}}\right) \tag{22}$$

and

$$0 = \varepsilon_{zz}\left(\omega_{\mathrm{LO}_{(n)}}\right). \tag{23}$$

Hence, LO modes with A_u symmetry are polarized along axis **b** only. LO modes with B_u symmetry are polarized within the **a**-**c** plane. The eigendisplacement vectors, $\hat{\mathbf{e}}_{\mathrm{LO}_{(n)}} = \cos\alpha_{\mathrm{LO}_{(n)}}\mathbf{x} + \sin\alpha_{\mathrm{LO}_{(n)}}\mathbf{y}$, can be found from

$$\tan\alpha_{\mathrm{LO}_{(n)}} = -\frac{\varepsilon_{xx}\left(\omega_{\mathrm{LO}_{(n)}}\right)}{\varepsilon_{xy}\left(\omega_{\mathrm{LO}_{(n)}}\right)} = -\frac{\varepsilon_{xy}\left(\omega_{\mathrm{LO}_{(n)}}\right)}{\varepsilon_{yy}\left(\omega_{\mathrm{LO}_{(n)}}\right)}. \tag{24}$$

For β-Ga_2O_3, in the absence of free charge carrier contributions, 4 LO modes with A_u symmetry and 8 LO modes with B_u symmetry are obtained from Eq. (22) and Eq. (23), respectively.

LPP mode determination. For β-Ga_2O_3, in the presence of free charge carrier contributions, Eq. (6) factorizes again into

$$0 = \varepsilon_{xx}\left(\omega_{\mathrm{LPP}_{(n)}}\right)\varepsilon_{yy}\left(\omega_{\mathrm{LPP}_{(n)}}\right) - \varepsilon_{xy}^2\left(\omega_{\mathrm{LPP}_{(n)}}\right) \tag{25}$$

and

$$0 = \varepsilon_{zz}(\omega_{\mathrm{LPP}_{(n)}}). \tag{26}$$

Hence, LPP modes with A_u symmetry are polarized along axis **b** only. LPP modes with B_u symmetry are polarized within the **a**-**c** plane. The eigendisplacement vectors, $\hat{\mathbf{e}}_{\mathrm{LPP}_{(n)}} = \cos\alpha_{\mathrm{LPP}_{(n)}}\mathbf{x} + \sin\alpha_{\mathrm{LPP}_{(n)}}\mathbf{y}$, can be found from

$$\tan\alpha_{\mathrm{LPP}_{(n)}} = -\frac{\varepsilon_{xx}\left(\omega_{\mathrm{LPP}_{(n)}}\right)}{\varepsilon_{xy}\left(\omega_{\mathrm{LPP}_{(n)}}\right)} = -\frac{\varepsilon_{xy}\left(\omega_{\mathrm{LPP}_{(n)}}\right)}{\varepsilon_{yy}\left(\omega_{\mathrm{LPP}_{(n)}}\right)}. \tag{27}$$

The presence of a free charge carrier plasma within β-Ga_2O_3 results in 5 LPP modes with A_u symmetry and 12 LPP modes with B_u symmetry, and which are obtained from Eq. (25) and Eq. (26), respectively.

Lyddane-Sachs-Teller relation. In the absences of free charge carriers, static and high-frequency dielectric constants fulfill the Lyddane-Sachs-Teller (LST) relation [49,53,54]

$$\frac{\varepsilon_{\mathrm{DC}}}{\varepsilon_{\infty}} = \prod_{l=1}^{m}\left(\frac{\omega_{\mathrm{LO},l}}{\omega_{\mathrm{TO},l}}\right)^2, \tag{28}$$

where m denotes the number of mode branches of a given material along a given major polarizability axis. The LST relation is derived from the behavior of a dielectric function at static and high frequencies where the imaginary part must vanish. Because the long-wavelength dielectric function can typically be rendered as a general response function with second-order poles and zeros, the summation of all zeros and poles at static frequency leads to Eq. (28). Written most commonly with the intent for isotropic materials, the relation has been found correct for anisotropic dielectrics with orthogonal axes [47,52,55]. It is also valid for the **b**-axis response, i.e., for ε_{zz} here.

For the **a**-**c** plane a physically meaningful set of dielectric functions along fixed orthogonal axes does not exist, and the relation in Eq. (28) is not generally valid for materials with monoclinic and triclinic crystal structures. However, a generalized relation for monoclinic materials can be found, analogous to the LST relation. Following the same logic in derivation, one may inspect the behavior of the subdeterminant of the monoclinic dielectric function tensor, $\varepsilon_{xx}\varepsilon_{yy} - \varepsilon_{xy}^2$. At zero frequencies, this function is equal to $\varepsilon_{\mathrm{DC},xx}\varepsilon_{\mathrm{DC},yy} - \varepsilon_{\mathrm{DC},xy}^2$; the high-frequency limit follows likewise. Casting the subdeterminant into a factorized form, it is crucial to recognize that all terms with $(\omega_{\mathrm{TO},(l)}^2 - \omega^2)^{-2}$ do not contribute to the summation because their amplitudes cancel. Hence, the denominator factorizes into the second-order poles at all B_u TO frequencies, and the numerator factorizes into all roots of the subdeterminant. The order of the polynomials are both $2m$; hence, there are m poles at $\omega_{\mathrm{TO},(l)}^2$ and m zeros at $\omega_{\mathrm{LO},(l)}^2$. The generalized LST relation for monoclinic materials reads then

$$\frac{\varepsilon_{\mathrm{DC},xx}\varepsilon_{\mathrm{DC},yy} - \varepsilon_{\mathrm{DC},xy}^2}{\varepsilon_{\infty,xx}\varepsilon_{\infty,yy} - \varepsilon_{\infty,xy}^2} = \prod_{l=1}^{m}\left(\frac{\omega_{\mathrm{LO},l}}{\omega_{\mathrm{TO},l}}\right)^2. \tag{29}$$

In the above equation, $m = 8$ denotes the number of modes with B_u symmetry for β-Ga_2O_3. While the implementation of the LST relation, or its generalization above, is not truly needed when analyzing long-wavelength ellipsometry data, the relations are quite useful to check for consistency of determined phonon and dielectric constant parameters.

C. Generalized ellipsometry

For optically anisotropic materials it is necessary to apply the generalized ellipsometry approach because coupling between the p (parallel to the plane of incidence) and s (perpendicular to the plane of incidence) polarized incident electromagnetic plane wave components occurs upon reflection off the sample surface. β-Ga_2O_3 possesses monoclinic crystal structure, and is highly anisotropic. In previous work, which included uniaxial and biaxial materials in single-layer and multiple-layer structures such as corundum [52], rutile [55], antimonite [56], pentacene [57,58], zinc metal oxides [59], wurtzite structure group-III nitride heterostructures [60–70], and form-induced anisotropic thin films [71], we discussed theory and applications of generalized ellipsometry in detail. In a number of recent publications we discussed the treatment and necessity of investigating off-axis cut surfaces from anisotropic crystals to gain access to all long-wavelength active phonon modes, for example in ZnO [72], and in wurtzite structure group-III nitrides [73–75]. A multiple sample, multiple azimuth, and multiple angle of incidence approach is required for β-Ga_2O_3. Hence, multiple single-crystalline samples cut under different angles from the same crystal must be investigated and analyzed simultaneously.

1. Mueller matrix formalism

In the generalized ellipsometry formalism, the interaction of electromagnetic plane waves with layered samples is described within the Jones or Mueller matrix formalism [47,48,76,77]. The Mueller matrix renders the optical sample properties at a given angle of incidence and sample azimuth, and data measured must be analyzed through a best-match model calculation procedure. In the generalized ellipsometry situation the Stokes vector formalism, where real-valued matrix elements connect the Stokes parameters of the electromagnetic plane waves before and after sample interaction, is an appropriate choice for casting the ellipsometric measurement parameters. The Stokes vector components are defined by $S_0 = I_p + I_s, S_1 = I_p - I_s, S_2 = I_{45} - I_{-45}, S_3 = I_{\sigma+} - I_{\sigma-}$, where $I_p, I_s, I_{45}, I_{-45}, I_{\sigma+}$, and $I_{\sigma-}$ denote the intensities for the p, s, $+45^\circ$, -45°, right-handed, and left-handed circularly polarized light components, respectively [50]. The Mueller matrix is defined by arranging incident and exiting Stokes vectors into matrix form:

$$\begin{pmatrix} S_0 \\ S_1 \\ S_2 \\ S_3 \end{pmatrix}_{\text{output}} = \begin{pmatrix} M_{11} & M_{12} & M_{13} & M_{14} \\ M_{21} & M_{22} & M_{23} & M_{24} \\ M_{31} & M_{32} & M_{33} & M_{34} \\ M_{41} & M_{42} & M_{43} & M_{44} \end{pmatrix} \begin{pmatrix} S_0 \\ S_1 \\ S_2 \\ S_3 \end{pmatrix}_{\text{input}}. \quad (30)$$

2. Ellipsometry data and model dielectric function analyses

Spectroscopic ellipsometry is an indirect method and requires detailed model analysis procedures in order to extract relevant physical parameters [78,79]. Here, the simple two-phase (substrate ambient) model is employed, where the substrate represents single-crystal β-Ga_2O_3 samples. The light propagation within the anisotropic substrate is calculated by applying a 4×4 matrix algorithm applicable to plane-parallel interfaces [80–82].

The matrix algorithm requires a full description of all dielectric function tensor elements of the substrate. In order to perform this description, coordinate relations must be established. Two coordinate systems must be related to each other, one that is tied to the instrument and another which must be tied to the crystallographic sample description. The system tied to the instrument is the system in which the dielectric function tensor must be cast into for the 4×4 matrix algorithm. We chose both coordinate systems to be Cartesian. The sample normal defines the laboratory coordinate system's $\hat{z}$ axis, which points into the surface of the sample [80]. The sample surface then defines the laboratory coordinate system's $\hat{x}$-$\hat{y}$ plane. The sample surface is at the origin of the coordinate system. The plane of incidence is the $\hat{x}$-$\hat{z}$ plane. Note that the system $(\hat{x}, \hat{y}, \hat{z})$ is defined by the ellipsometer instrumentation through the plane of incidence and the sample holder. One may refer to this system as the laboratory coordinate system. The system (x, y, z) in Fig. 1 is fixed by our choice to the specific orientation of the β-Ga_2O_3 crystal axes shown in Fig. 2. One may refer to system (x, y, z) as our β-Ga_2O_3 system. Then, the full dielectric tensor in the 4×4 matrix algorithm is obtained by setting $\varepsilon_{xx}, \varepsilon_{xy}, \varepsilon_{yy}$, and ε_{zz} as unknown parameters, and by setting the remaining elements to zero.

Then, according to the crystallographic surface orientation of a given sample, and according to its azimuth orientation relative to the plane of incidence, an Euler angle rotation is applied to ε. The definition of the Euler angle parameters between two Cartesian coordinate systems is shown in Fig. 3. The Euler parameters describe the angular rotations of the β-Ga_2O_3 crystal axes depicted in Fig. 2 relative to the laboratory (ellipsometer) coordinate system for every ellipsometry measurement. Matrix A is obtained by

$$A = R_1(\varphi) R_2(\theta) R_1(\psi), \quad (31)$$

with

$$R_1(v) = \begin{pmatrix} \cos v & -\sin v & 0 \\ \sin v & \cos v & 0 \\ 0 & 0 & 1 \end{pmatrix}, \quad (32)$$

$$R_2(v) = \begin{pmatrix} 1 & 0 & 0 \\ 0 & \cos v & -\sin v \\ 0 & \sin v & \cos v \end{pmatrix}. \quad (33)$$

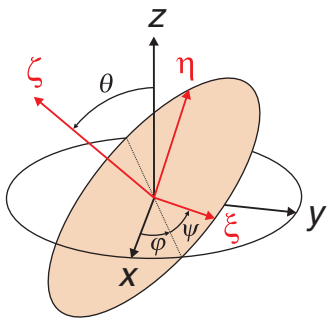

FIG. 3. Definition of the Euler angles φ, θ, and ψ and the orthogonal rotations as provided by **A**. (ξ, η, ζ) and (x, y, z) refer to the Cartesian auxiliary and laboratory coordinate systems, respectively. Redrawn from Ref. [47].

The sample azimuth angle, typically termed φ, is defined by a certain in-plane rotation with respect to the sample normal. The sample azimuth angle describes the mathematical rotation that a model dielectric function tensor of a specific sample must make when comparing calculated data with measured data from one or multiple samples taken at multiple, different azimuth positions. For example, for a (010) surface cut, Euler angles θ and ψ are zero, the **a**-**c** plane is the surface of the sample, and $\varphi = 0$ when axis **a** points along the plane of incidence. Vector $\mathbf{c}^\star$ is then perpendicular to the plane of incidence.

As a first step in data analysis, all ellipsometry data were analyzed using a wavelength-by-wavelength approach. Thereby, all data obtained at the same wave number from multiple samples, multiple azimuth angles, and multiple angles of incidence are included (polyfit) and one set of complex values $\varepsilon_{xx},\varepsilon_{xy},\varepsilon_{yy}$, and ε_{zz} is searched for. This procedure is simultaneously performed for all wavelengths, while results of $\varepsilon_{xx},\varepsilon_{xy},\varepsilon_{yy}$, and ε_{zz} for one wavelength have no influence on results at any other wavelength. In addition, each sample requires one set of 3 independent Euler angle parameters. The latter describe the rotations of the β-Ga_2O_3 auxiliary coordinate system at zero azimuth. Zero azimuth is the first azimuth position at which measurements were performed. Multiple azimuth positions differ by 45° counterclockwise increments. These increments are added to Euler angle parameter φ, and hence once the zero azimuth position parameter is known all other Euler parameters are known. In this polyfit and wavelength-by-wavelength approach, we have not augmented any physical line shape assumptions for the spectral behavior of $\varepsilon_{xx},\varepsilon_{xy},\varepsilon_{yy}$, and ε_{zz}. In a second step, $\varepsilon_{xx},\varepsilon_{xy},\varepsilon_{yy}$, and ε_{zz} are analyzed simultaneously by Eqs. (21). As a result, we obtain all parameters for TO, LO, and LPP modes as well as for static and high-frequency dielectric constants.

Two regression analyses (Levenberg-Marquardt algorithm) are performed. The first is minimizing the difference between measured and calculated generalized ellipsometry data during the polyfit. The second is minimizing the difference between the wavelength-by-wavelength extracted $\varepsilon_{xx},\varepsilon_{xy},\varepsilon_{yy}$, and ε_{zz} spectra and those calculated by Eqs. (21). All model parameters were varied until calculated and experimental data matched as closely as possible (best-match model). This is done by minimizing the mean-squared error (χ^2) function which is weighed to estimated experimental errors (σ) determined by the instrument for each data point [38,47,52,55,81]. For the second regression step, the numerical uncertainty limits of the 90% confidence interval from the first regression were used as experimental error bars for the wavelength-by-wavelength extracted $\varepsilon_{xx},\varepsilon_{xy},\varepsilon_{yy}$, and ε_{zz} spectra. A similar approach was described, for example, in Refs. [47,52,55,83]. All best-match model calculations were performed using WVASE32 (J. A. Woollam Co., Inc.).

D. Phonon mode calculations

Theoretical calculations of long-wavelength active Γ-point phonon frequencies were performed by plane wave density functional theory (DFT) using Quantum ESPRESSO (QE) [84]. The exchange correlation functional of Perdew and Zunger (PZ) [85] and norm-conserving pseudopotentials from the QE library were implemented. A primitive cell of β-Ga_2O_3 consisting of six oxygen and four gallium atoms was first relaxed to force levels less than 1/1000 Ry/bohr. A dense $4 \times 8 \times 16$ regular Monkhorst-Pack grid was used for sampling of the Brillouin zone [86]. A convergence threshold of 1×10^{-12} was used to reach self-consistency with a large electronic wave function cutoff of 100 Ry. The phonon frequencies were computed at the Γ point of the Brillouin zone using density functional perturbation theory [87]. We modified the code of QE to provide, in addition to phonon frequencies and their infrared transition dipoles, the actual Cartesian components of the infrared transition dipole moments (square of the transition dipole). This allows us to analyze projections of the infrared transition dipoles onto arbitrary crystallographic axes and planes. The results of the phonon mode calculations for infrared active modes with A_u and B_u symmetry are listed in Table I. Data listed include the TO resonance frequencies, and for modes with B_u symmetry the angles of the transition dipoles relative to axis **a** within the **a**-**c** plane. Renderings of molecular displacements for each mode were prepared using XCrysDen [88,89] running under Silicon Graphics Irix 6.5, and are shown in Fig. 4.

III. EXPERIMENT

Single crystals of β-Ga_2O_3 were grown by the edge-defined film-fed growth method described in Refs. [90–92] at Tamura Corp., Japan. The substrates were fabricated by slicing from bulk crystals according to their intended surface orientation, and then single-side polished. The substrate dimensions are 650 μm × 10 mm × 10 mm. The substrates are Sn doped with an estimated activated electron density of $N_d - N_a \approx (2\text{–}9) \times 10^{18}$ cm^{-3}.

The vibrational properties and free charge carrier properties of β-Ga_2O_3 were studied by room temperature infrared (IR) and far-infrared (FIR) GSE. The IR-GSE

TABLE I. Phonon mode parameters for A_u and B_u modes obtained from DFT calculations using Quantum ESPRESSO. Renderings of displacements are shown in Fig. 4. The unit cell parameters are found as $a = 12.19$ Å, $b = 3.016$ Å, $c = 5.75$ Å, and $\beta = 103.59°$, in agreement with Ref. [44].

		$X = B_u$								$X = A_u$			
Parameter		$k = 1$	2	3	4	5	6	7	8	$k = 1$	2	3	4
A_k^X	This work	4.65	9.48	30.57	28.1	5.37	0.89	7.33	10.43	12.76	23.24	14.34	0.07
$\omega_{\mathrm{TO},k}$ (cm^{-1})	This work	753.76	705.78	589.86	446.83	365.84	289.71	260.4	202.4	678.39	475.69	327.45	155.69
$\alpha_{\mathrm{TO},k}$ (deg)	This work	70.9	25.0	128	46.1	165	7.5	175	101				
$\omega_{\mathrm{TO},k}$ (cm^{-1})	Ref. [28]	741.6	672.6	574.3	410.5	343.6	265.3	251.6	187.5	647.9	383.5	296.2	141.6

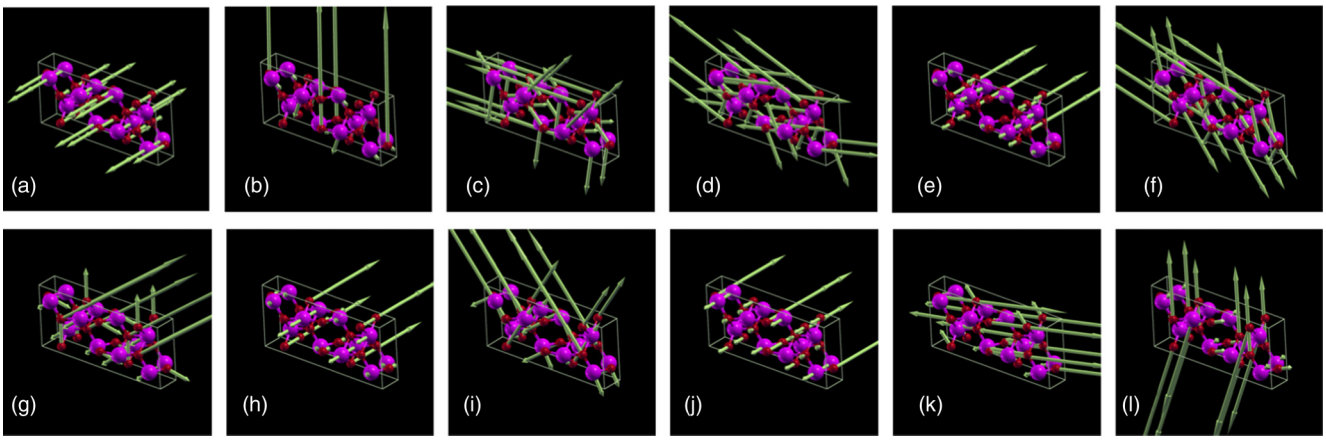

FIG. 4. Renderings of TO phonon modes in β-Ga_2O_3 with A_u [(a) $A_u(4)$, (e) $A_u(3)$, (h) $A_u(2)$, (j) $A_u(1)$] and B_u symmetry [(b) $B_u(8)$, (c) $B_u(7)$, (d) $B_u(6)$, (f) $B_u(5)$, (g) $B_u(4)$, (i) $B_u(3)$, (k) $B_u(2)$, (l) $B_u(1)$]. The respective phonon mode frequency parameters calculated using Quantum ESPRESSO are given in Table I. The renderings were prepared using XCrysDen [88,89].

measurements were performed on a rotating compensator infrared ellipsometer (J. A. Woollam Co., Inc.) in the spectral range of 500–1500 cm^{-1} with a spectral resolution of 2 cm^{-1}. The FIR-GSE measurements were performed on an in-house-built rotating-polarizer rotating-analyzer far-infrared ellipsometer in the spectral range of 50–500 cm^{-1} with an average spectral resolution of 1 cm^{-1} [93]. All GSE measurements were performed at 50°, 60°, and 70° angles of incidence. All measurements are reported in terms of Mueller matrix elements, which are normalized to element M_{11}. Note that due to the lack of a compensator for the FIR range in this work, no elements of the fourth row or column are reported for the FIR range. In order to acquire sufficient information to differentiate and determine $\varepsilon_{xx}, \varepsilon_{xy}, \varepsilon_{yy}$, and ε_{zz}, data measured from at least two differently cut surfaces of β-Ga_2O_3 and within at least two different azimuth positions are needed. Here, we investigate a (010) and a $(\bar{2}01)$ sample. At least 5 azimuth positions were measured on each sample, separated by 45°.

IV. RESULTS AND DISCUSSION

A. Dielectric function tensor analysis

Figures 5 and 6 summarize experimental and best-match model calculated data for the (010) and $(\bar{2}01)$ surfaces investigated in this work. Insets in Figs. 5 and 6 show schematically the sample surface, the plane of incidence, and the orientation of axis **b**. Graphs depict selected data, obtained at 3 different sample azimuth orientations each 45° apart. Panels with individual Mueller matrix elements are shown separately, and individual panels are arranged according to the indices of the Mueller matrix element. It is observed by experiment as well as by model calculations that all Mueller matrix elements are symmetric, i.e., $M_{ij} = M_{ji}$. Hence, elements with $M_{ij} = M_{ji}$, i.e., from upper and lower diagonal parts of the Mueller matrix, are plotted within the same panels. Therefore, the panels represent the upper part of a 4×4 matrix arrangement. Because all data obtained are normalized to element M_{11}, and because $M_{1j} = M_{j1}$, the first column does not appear in this arrangement. The only missing element is M_{44}, which cannot be obtained in our current instrument configuration due to the lack of a second compensator. Data are shown for wave numbers (frequencies) from 125 cm^{-1} to 1200 cm^{-1}, except for column $M_{4j} = M_{j4}$, which only contains data from approximately 250 cm^{-1} to 1200 cm^{-1}. All other panels show data obtained within the FIR range (125 cm^{-1} to 500 cm^{-1}) using our FIR instrumentation and data obtained within the IR range (500 cm^{-1} to 1200 cm^{-1}) using our IR instrumentation. Data from the additional azimuth orientations (at least 2) for each sample are not shown.

While every data set (sample, position, azimuth, angle of incidence) is unique, all data sets share characteristic features at certain wavelengths. These wavelengths are indicated by vertical lines. As discussed further below, all lines are associated with TO or LPP modes with A_u and B_u symmetry. While we do not show all data in Figs. 5 and 6 for brevity, we note that all data sets possess a twofold azimuth symmetry; i.e., all data sets are identical when a sample is measured again shifted by 180° azimuth orientation. The most notable observation from the experimental Mueller matrix data behavior is the strong anisotropy which is reflected by the nonvanishing off-diagonal block elements M_{13}, M_{23}, M_{14}, and M_{24}, and the strong dependence on sample azimuth in all elements. A noticeable observation is that the off-diagonal block elements in position P1 for the $(\bar{2}01)$ surface in Fig. 6 are close to zero. There, axis **b** is aligned almost perpendicular to the plane of incidence. Hence, the monoclinic plane with **a** and **c** is nearly parallel to the plane of incidence, and as a result almost no conversion of p to s polarized light occurs and vice versa. As a result, the off-diagonal block elements of the Mueller matrix are near zero. The reflected light for s polarization is determined by ε_{zz} alone, while the p polarization receives contributions from $\varepsilon_{xx}, \varepsilon_{xy}$, and ε_{yy}, which then vary with the angle of incidence. Analysis of such data hence still requires the monoclinic model approach as discussed in this paper.

All data were analyzed simultaneously during the poly-fit, best-match model data regression procedure. For every wavelength, up to 330 independent data points were included from the different samples, azimuth positions, and angles of incidence, while only 8 independent parameters for $\varepsilon_{xx}, \varepsilon_{xy}, \varepsilon_{yy}$, and ε_{zz} were searched for. In addition, two sets of 3 wavelength-independent Euler angle parameters were looked

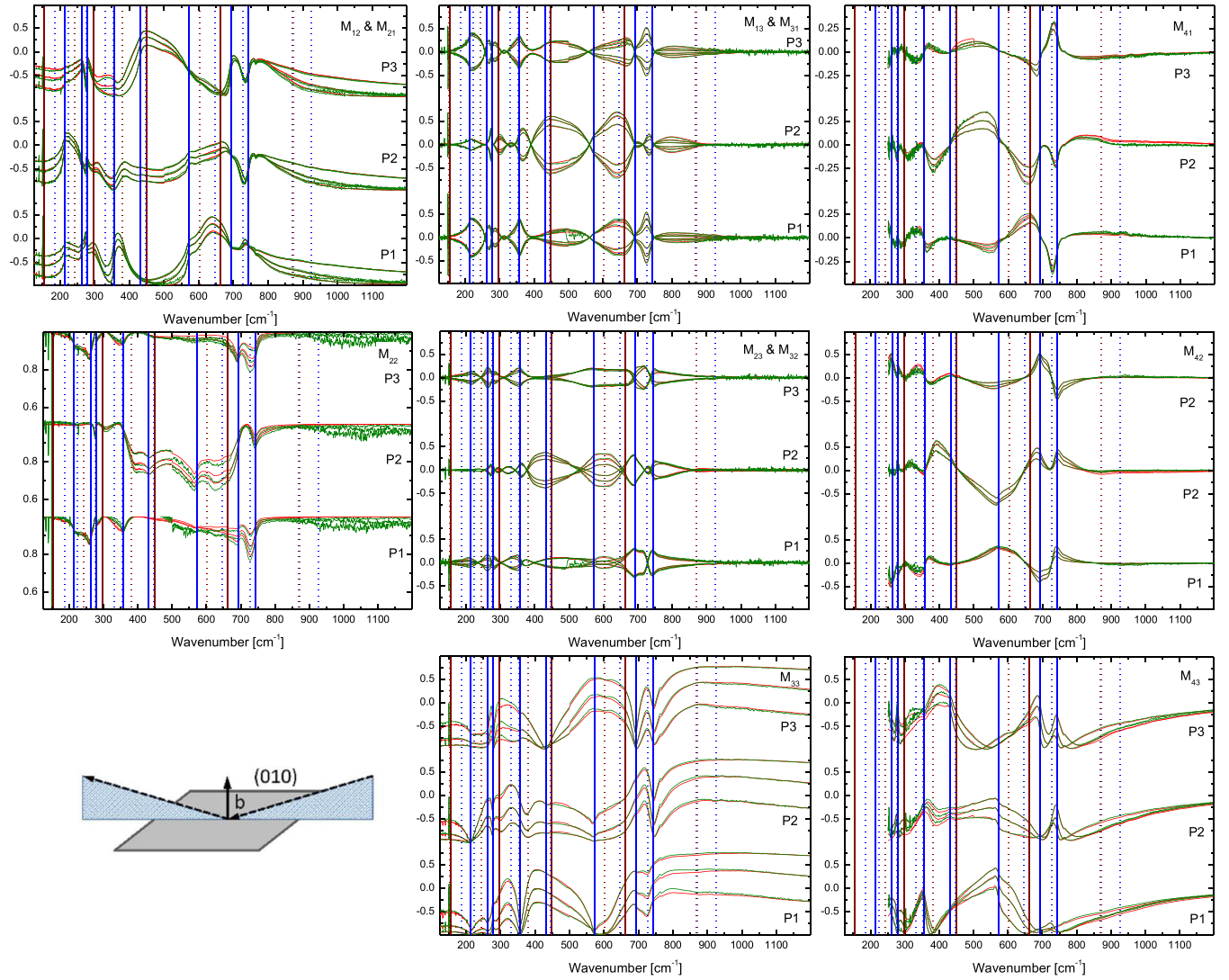

FIG. 5. Experimental (dotted green lines) and best match model calculated (solid red lines) Mueller matrix data obtained from a (010) surface at three different sample azimuth orientations [P1: $\varphi = 62.5(4)^\circ$, P2: $\varphi = 107.5(4)^\circ$, P3: $\varphi = 152.5(4)^\circ$]. Data were taken at three angles of incidence ($\Phi_a = 50^\circ, 60^\circ, 70^\circ$). Equal Mueller matrix data, symmetric in their indices, are plotted within the same panels for convenience. Vertical lines indicate wave numbers of TO (solid lines) and LPP modes (dotted lines) with B_u symmetry (blue) and A_u symmetry (brown). Fourth-column elements are only available from the IR instrument. Note that all elements are normalized to M_{11}. The remaining Euler angle parameters are $\theta = 0.4(2)$ and $\psi = 0.0(1)$, consistent with the crystallographic orientation of the (010) surface. The inset depicts schematically the sample surface, the plane of incidence, and the orientation of axis **b**.

for. The results of this calculation are shown in Figs. 5 and 6 as solid lines for the Mueller matrix elements, and in Figs. 7, 8, 9, and 10 as dotted lines for $\varepsilon_{xx}, \varepsilon_{xy}, \varepsilon_{yy}$, and ε_{zz}, respectively. In Figs. 5 and 6 the agreement between measured and model-calculated data is excellent. The Euler angle parameters, given in the captions of Figs. 5 and 6, are in excellent agreement with the anticipated orientations of the crystallographic sample axes. For example, measurement on sample (010) initiated with axis **b** parallel to $\hat{z}$ and a natural cleavage edge parallel to **c** was oriented approximately such that axis **a** had an $\approx 60^\circ$ azimuth angle with respect to the plane of incidence.

To begin with, distinct features in $\varepsilon_{xx}, \varepsilon_{xy}, \varepsilon_{yy}$, and ε_{zz} can be discussed without further model line shape calculations. Vertical lines are drawn into Figs. 7–10 to indicate extrema in the imaginary parts of each element. One can observe that these vertical lines are identical for $\varepsilon_{xx}, \varepsilon_{xy}$, and ε_{yy}, while a different set is seen for ε_{zz}. There are 8 distinct frequencies in $\varepsilon_{xx}, \varepsilon_{xy}$, and ε_{yy}, and 4 in ε_{zz}. These frequencies indicate TO modes with B_u and A_u symmetry. The vertical line indexed with "6" in $\varepsilon_{xx}, \varepsilon_{xy}$, and ε_{yy} is associated with a resonance feature which seems to only occur in ε_{xx}. This indicates a mode with polarization along direction **a** only, while all other lines indicate modes which are polarized purely along neither **a** nor $\mathbf{c}^\star$. We further note the asymptotic increase towards longer wavelengths in the imaginary parts of $\varepsilon_{xx}, \varepsilon_{yy}$, and ε_{zz}. This increase is likely caused by free charge carrier contributions. No such behavior is seen in ε_{xy}.

B. Phonon mode analysis

The imaginary parts of $\varepsilon_{xx}, \varepsilon_{yy}$, and ε_{zz} show features which can typically be rendered by the Lorentzian broadened

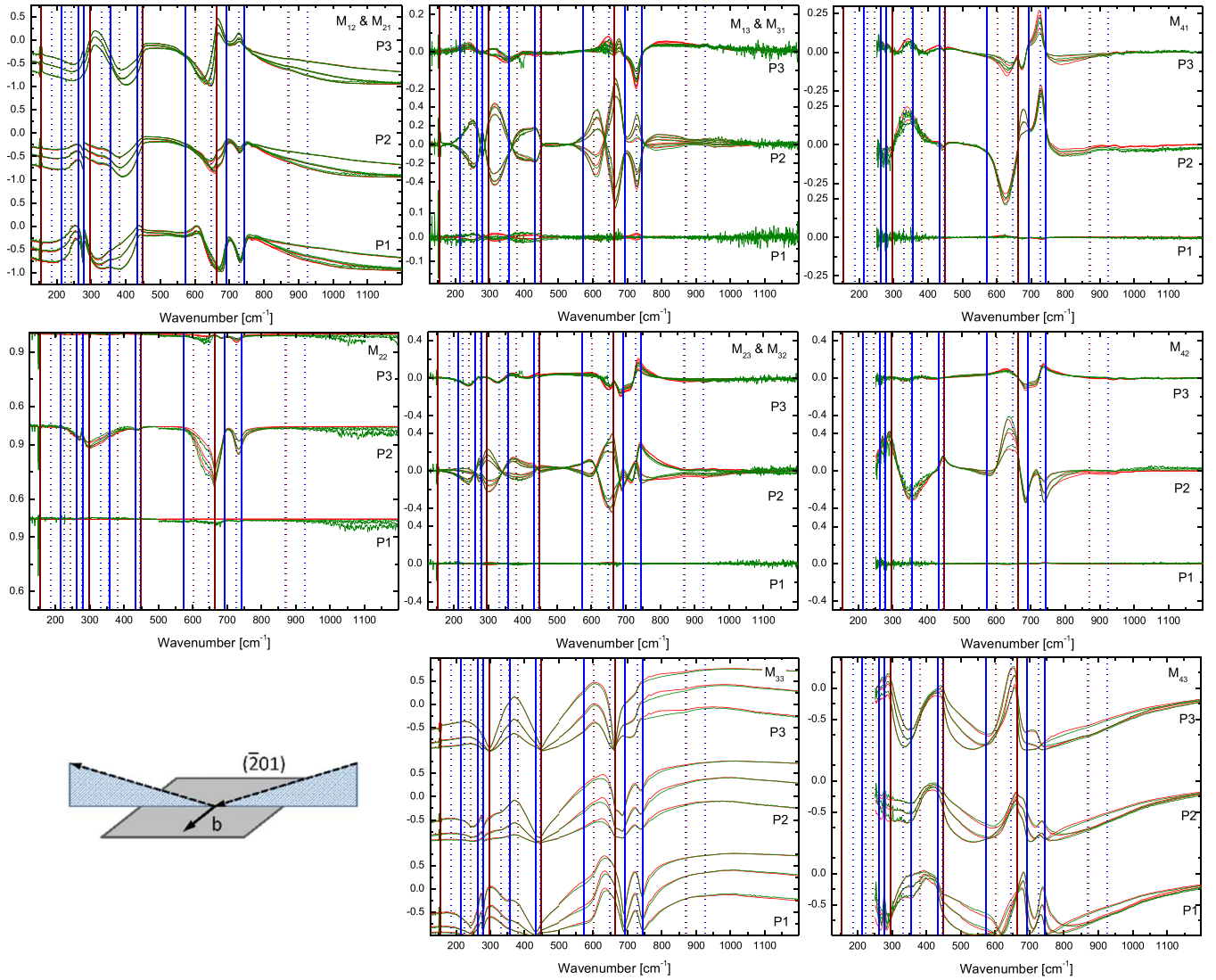

FIG. 6. Same as Fig. 5 for the $(\bar{2}01)$ sample at azimuth orientation P1: $\varphi = 179.(3)^\circ$, P2: $\varphi = 224.(3)^\circ$, P3: $\varphi = 269.(3)^\circ$. $\theta = 90.(5)$ and $\psi = -28.(1)$, consistent with the crystallographic orientation of the $(\bar{2}01)$ surface. Note that in position P1, axis **b** which is parallel to the sample surface in this crystal cut is aligned almost perpendicular to the plane of incidence. Hence, the monoclinic plane with **a** and **c** is nearly parallel to the plane of incidence, and as a result almost no conversion of p to s polarized light occurs and vice versa. As a result, the off-diagonal block elements of the Mueller matrix are near zero. The inset depicts schematically the sample surface, the plane of incidence, and the orientation of axis **b**, shown approximately for position P1.

harmonic oscillator functions in Eq. (3). With our model introduced in Sec. II A we obtain best-match model calculations, which are also shown in Figs. 7–10. Again, an excellent match between the wavelength-by-wavelength determined dielectric function tensor elements and our physical model line shape rendering is noted. It is worthwhile noting that the wavelength-by-wavelength derived dielectric functions are all Kramers-Kronig consistent since the Lorentzian-broadened harmonic oscillator functions are Kramers-Kronig consistent. We have thereby independently verified that all tensor components of β-Ga_2O_3 are Kramers-Kronig consistent. The best-match model line shape calculation parameters are summarized in Table II. As a result, we obtain phonon mode parameters for TO, LO, and LPP modes.

TO modes. We find 8 TO mode frequencies within elements ε_{xx},ε_{xy}, and ε_{yy}. These are the modes with B_u symmetry. The vertical lines and mode indices in Figs. 7, 8, and 9 are located at frequencies which are identical to frequencies for ω_{TO} listed in Table II. As discussed in Sec. II B, element ε_{xy} provides insight into the relative orientation of the unit eigendisplacement vectors for each TO mode within the **a**-**c** plane. In particular, modes B_u-3, B_u-5, and B_u-7 cause negative imaginary resonance features in ε_{xy}. Accordingly, their unit eigendisplacement vectors in Table II reflect values larger than 90°. Modes B_u-1, B_u-2, B_u-4, B_u-6, and B_u-8 possess values less than 90°. Accordingly, their resonance features in the imaginary part of ε_{xy} are positive. However, mode B_u-6 does not cause a detectable resonance feature in the imaginary part of ε_{xy} because its unit eigendisplacement vector is almost parallel to x. Mode B_u-2 is almost parallel to mode B_u-6, but its amplitude is much larger. Hence, a small feature from mode B_u-2 is detected in ε_{xy} here. As predicted by the model

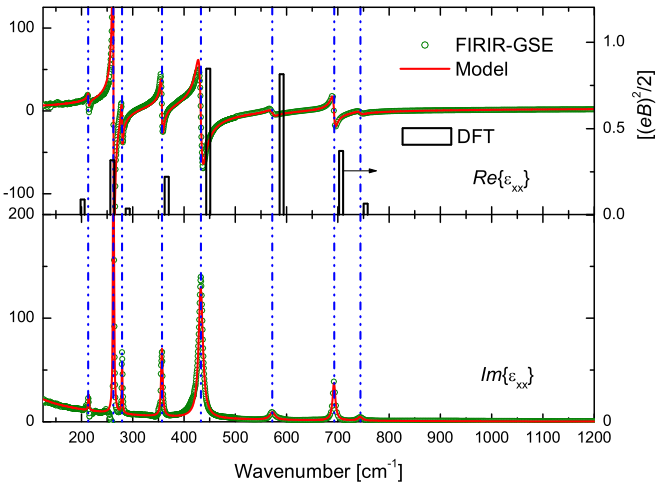

FIG. 7. Dielectric function tensor element ε_{xx}, representative for axis **a**. Lines indicate results from wavelength by wavelength best match model calculation to experimental Mueller matrix data (dotted green) and best match model line shape analysis (solid red). Vertical lines indicate B_u mode TO frequencies. Vertical bars indicate DFT-calculated infrared transition dipole moments projected onto axis **a** in atomic units.

description in this work, resonances nearly parallel to x reveal features mostly in ε_{xx} and merely or none in ε_{yy}. This is verified by our experimental finding here. A schematic presentation of the oscillator function amplitude parameters $A_k^{B_u}$ and the orientation according to angles $\alpha_{\mathrm{TO},k}$ from Table II within the **a**-**c** plane is shown in Fig. 11(a).

The TO mode frequencies and their unit eigendisplacement vectors obtained from the ellipsometry model analysis are in very good agreement with the DFT phonon mode calculations shown in Table I. Predicted mode frequencies agree within a few wave numbers with the experimental findings. The DFT-calculated phonon mode infrared transition dipole moments (oscillator strengths) projected onto axes **a**,**c***, and **b** are shown

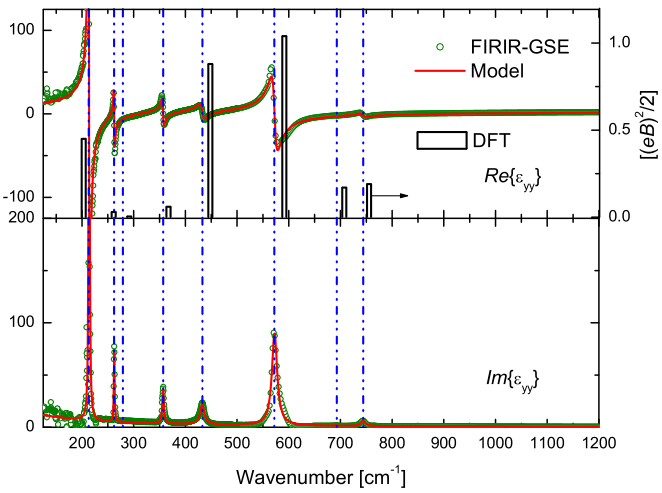

FIG. 8. Same as Fig. 7 for ε_{yy}, representative for polarization along direction **c***. Vertical bars indicate DFT-calculated infrared transition dipole moments projected onto axis **c***.

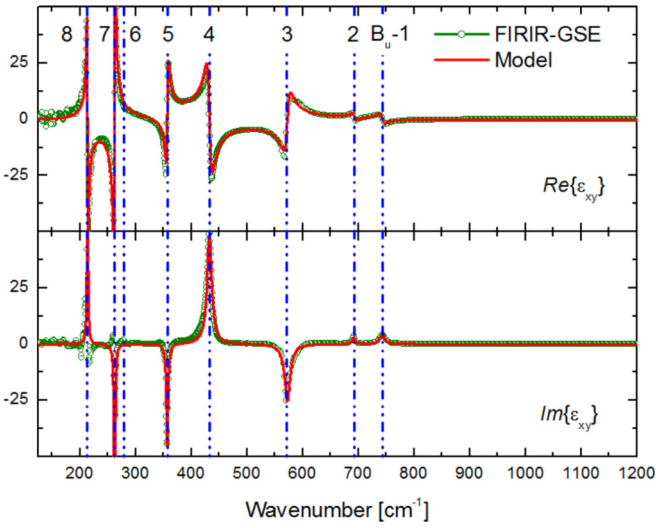

FIG. 9. Same as Fig. 7 for ε_{xy}, the shear transformation element within the **a**-**c** plane. Numerals index B_u mode TO frequencies.

in Figs. 7, 8, and 10, respectively, as vertical bars. The bars are located at the DFT-calculated frequencies of the TO modes. The magnitude of the absorption features within the imaginary parts of the dielectric function tensor elements, which are proportional to the oscillator function amplitude parameters $A_k^{B_u}$ and projections by angles $\alpha_{\mathrm{TO},k}$, are comparable with the DFT-calculated phonon mode infrared transition amplitudes. The DFT-calculated dielectric displacement amplitudes are obtained in atomic units $[(eB)^2/2$, where B is the Bohr length]. The projected infrared transition dipole moments are in good relative agreement when compared with the amplitudes of the Lorentz oscillator functions for the A_u and B_u modes found from the ellipsometry analysis. Figure 11(b) depicts projections of the predicted infrared transition dipole moments (intensities) onto axes **a** and **c***, in analogy to projected oscillator amplitudes found from the ellipsometry analysis

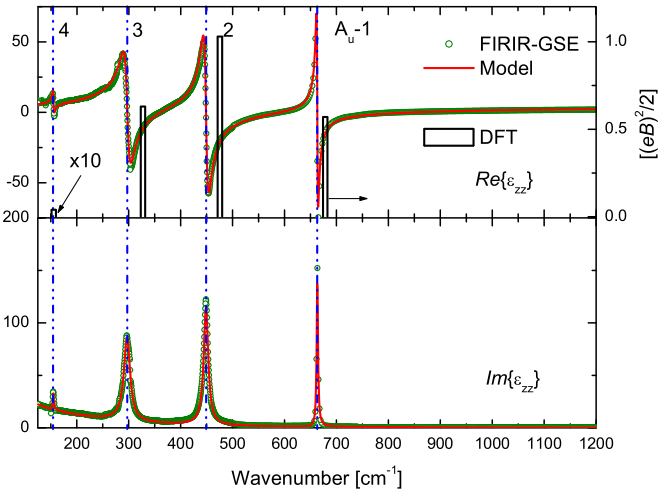

FIG. 10. Same as Fig. 7 for ε_{zz}, representative for polarization along axis **b**. Vertical lines indicate A_u mode TO frequencies. Vertical bars indicate DFT-calculated infrared transition dipole moments projected onto axis **b**.

TABLE II. TO and LO phonon parameters for A_u and B_u modes obtained from best match model analysis of ε_{xx},ε_{xy},ε_{yy}, and ε_{zz}. Also shown are the eigenvector polarization angles for B_u LO modes. The last digit which is determined within the 90% confidence interval is indicated with parentheses. Also included are data from recent IR reflectance measurements and phonon mode calculations. Data in square brackets were deduced assuming isotropic reflectance likely leading to erroneous TO parameters.

	$X = B_u$								$X = A_u$			
Parameter	$k = 1$	2	3	4	5	6	7	8	$k = 1$	2	3	4
A_k^X (cm^{-2})	266.(2)	406.(5)	821.(9)	795.(7)	365.(8)	164.(1)	485.(7)	520.(7)	544.(9)	727.(1)	592.(1)	7(8)
$\omega_{\mathrm{TO},k}$ (cm^{-1})	743.4(8)	692.4(4)	572.5(2)	432.5(7)	356.7(9)	279.1(5)	262.3(4)	213.7(9)	663.1(7)	448.6(6)	296.6(3)	154.8(4)
$\gamma_{\mathrm{TO},k}$ (cm^{-1})	11.(0)	6.5(5)	12.3(6)	10.1(3)	3.8(3)	1.9(8)	1.7(5)	1.(9)	3.(2)	10.(5)	14.(9)	2.(4)
$\alpha_{\mathrm{TO},k}$ (deg)	47.(8)	5.(1)	10(6)	21.(0)	14(4)	(4)	158.(5)	80.(9)				
$\omega_{\mathrm{LO},k}$ (cm^{-1})	81(0)	77(0)	70(9)	59(5)	38(9)	30(5)	28(6)	26(9)	781.(3)	562.(8)	345.(9)	156.(3)
$\alpha_{\mathrm{LO},k}$ (deg)	7(3)	−3(0)	(6)	7(3)	−3(1)	−4(2)	2(1)	2(7)				
$\omega_{\mathrm{TO},k}$ (cm^{-1})	[779][a]	[737][a]	[631][a]	[537][a]	[372][a]	[298][a]	[276][a]	[223][a]	660[b]	449[b]	295[b]	≈220[b]
$\omega_{\mathrm{LO},k}$ (cm^{-1})	746.6[c]	728.2[c]	625.3[c]	484.7[c]	354.1[c]	283.6[c]	264.5[c]	190.5[c]	738.5[c]	510.6[c]	325.5[c]	146.5[c]

[a]IR reflectance‖ c, Ref. [21].
[b]IR reflectance‖ b, Ref. [21].
[c]Theory, Ref. [28].

and shown in Fig. 11(a). Overall, the agreement between the TO mode eigendisplacement vector distribution within the **a**-**c** plane obtained from GSE and DFT results is very good. It is worth noting that the angular sequence of the B_u mode eigenvectors is in exact agreement. Calculated angles α agree within less than 25° of those found from our model analysis of the dielectric function tensor elements. In further agreement, modes B_u-3, B_u-5, and B_u-7 are predicted by theory to show the experimentally observed angular values larger than 90°, and modes B_u-1, B_u-2, and B_u-4 reveal by experiment the predicted angular values less than 90°. We find mode B_u-8 slightly below 90° while DFT predicts this mode slightly above 90°. Mode B_u-6, which we find nearly parallel to axis **a**, has a DFT-predicted value of ≈8°, in agreement with our experimental finding. Note that the eigendisplacement vectors describe a unipolar property without a directional assignment. Hence, α and $\alpha \pm \pi$ render equivalent eigendisplacement orientations.

LO modes. Using Eq. (6) one can calculate the intrinsic LO modes, that is, the LPP modes in the absence of free charge carriers. The free charge carrier properties are discussed further below. Subtracting the effects of the free charge carriers from the model functions for ε_{xx},ε_{xy},ε_{yy}, and ε_{zz}, the LO modes with B_u and A_u symmetry follow from Eqs. (22) and (23), respectively. We find 4 LO modes with A_u and 8 LO modes with B_u symmetry. Their values are summarized in Table II. B_u symmetry modes are also indicated in Fig. 12 at $\omega_p = 0$.

In materials with multiple phonon modes, typically the TO-LO rule holds; i.e., a TO mode is always followed by an LO mode with increasing frequency (wave number). We note that the TO-LO rule is fulfilled for modes with A_u symmetry, but not for B_u symmetry (Fig. 12). This observation can be understood by inspecting the unit eigendisplacement vectors. These are all parallel for TO and LO modes with A_u symmetry. Hence, the displacement pattern at which the net displacement charge sum is zero (LO mode) occurs above a TO frequency, and is bound by the next TO frequency. The TO-LO splitting only depends on the polarity of the TO resonance. The polarity expresses itself as the amplitude of the TO resonance. At any TO resonance, the net displacement charge is nonzero, and changes from positive to negative when moving across the TO frequency. Because the displacement patterns are disjunct between TO and LO modes, an LO mode cannot move across a TO mode, for example when the amplitudes of TO modes change. On the contrary, each TO and LO mode has a different orientation for modes with B_u symmetry. In crystals with monoclinic symmetry, the TO-LO pattern distribution is 2-dimensional. The LO mode charge oscillations do not necessarily share the same direction with the TO oscillations. Hence, an LO mode pattern may form at a frequency which is larger than those from a pair of TO modes, if the TO modes each have different angles with each other as well as with the LO oscillation. The vectors for the LO modes with B_u symmetry are shown in Fig. 13 at $\omega_p = 0$.

Liu, Mu, and Liu studied the lattice dynamical properties of β-Ga_2O_3 by using density functional perturbation theory [28]. The TO modes are included in Table I for comparison with our theoretical calculation results. The modes agree reasonably well, except for A_u-2 (see Table II). However, for the latter mode our theoretical results are much closer to our experimental results than the theoretical calculation in Ref. [28]. We further included calculated LO modes from Ref. [28] in Table II; however, we find their values are not in agreement at all with our experimental findings.

Víllora *et al.* investigated single crystals of β-Ga_2O_3 grown by the floating-zone technique [21]. Polarized reflectance spectra with an incidence angle of about 10° and in the 50–1200 cm^{-1} spectral region revealed 12 long-wavelength active modes, and contributions due to free charge carriers. The authors reported TO mode parameters and plasma parameters, and compared with measurements of the electrical conductivity and the electrical Hall coefficient. Platelet samples with surface (100) orientation allowed reflectance measurements with polarization along axes **b** and **c**. Not all modes could be resolved in all samples, and uncertainty limits were not provided. The TO mode frequencies obtained in our present work agree excellently with modes reported for A_u symmetry in Ref. [21]. However, the TO mode frequencies for B_u symmetry reported by Víllora *et al.* deviate substantially from those found in this present work (Table II). We explain this

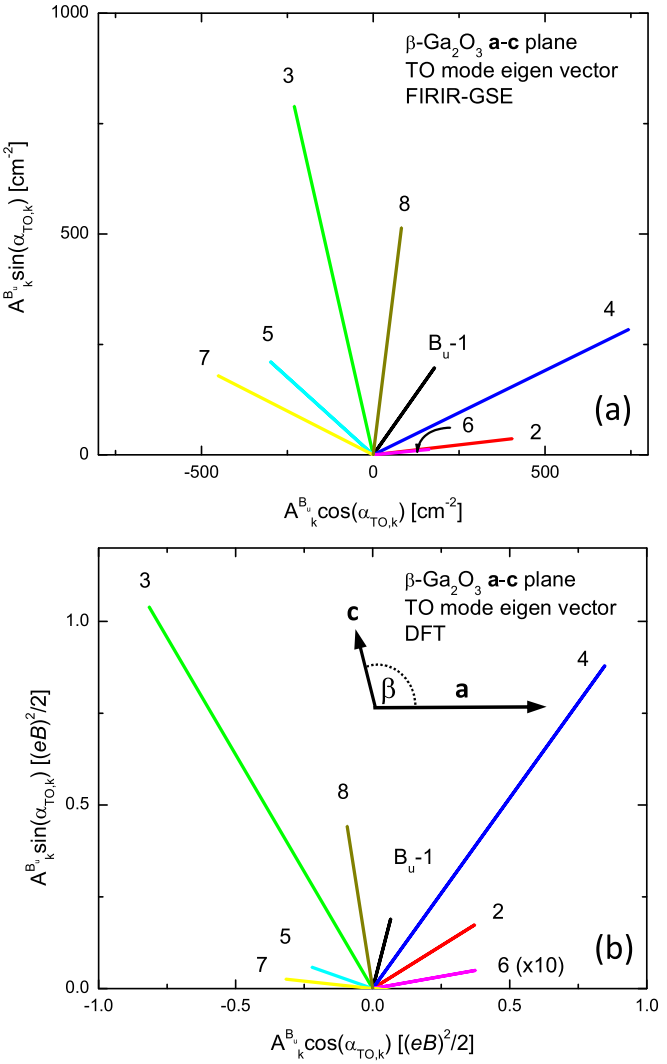

FIG. 11. (a) Schematic presentation of the B_u mode TO eigendisplacement orientation within the **a**-**c** plane according to TO mode amplitude parameters $A_k^{B_u}$ and orientation angles $\alpha_{\mathrm{TO},k}$ with respect to x obtained from GSE analysis (Table II). (b) DFT-calculated B_u mode TO phonon mode infrared transition dipoles (intensities) in coordinates of axes **a** and **c***. The transition dipole strength for mode B_u-6 is multiplied by 10 for convenience. The x axis is parallel to **a**; the y axis is parallel to **c***.

substantial difference by the fact that the authors ignored the anisotropy in the monoclinic β-Ga_2O_3 samples. Instead, the authors assumed that the measured reflectance spectra for polarization along axes **b** and **c** can be analyzed individually by using isotropic Fresnel equations for model calculations. While this assumption is correct for polarization parallel to axis **b** (but valid at normal incidence only), it is incorrect for polarization along **c** regardless of the angle of incidence. For the latter case, the isotropic model cannot correctly account for contributions that originate from ε_{xy}. As a result, incorrect virtual resonance features appear when matching Lorentzian line shapes to the measured reflectance data. We strongly believe that this explains the substantial deviations between the modes reported by Víllora *et al.* and the modes reported in this work. Bermudez and Prokes investigated β-Ga_2O_3

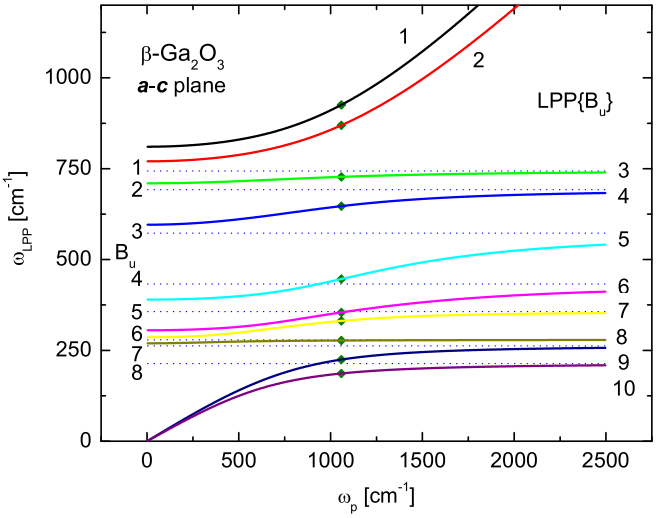

FIG. 12. LPP coupled modes polarized within the **a**-**c** plane as a function of isotropic plasma frequency ω_p. The horizontal lines indicate the frequencies of the B_u symmetry TO modes. Observed here is the deviation from the so called TO-LO rule usually observed in semiconductor materials with orthogonal eigenpolarization systems, which is no longer valid for monoclinic lattices. Symbols (diamonds) indicate the LPP mode frequencies observed in FIR-GSE and IR-GSE spectra in this work. Numbering of modes as shown in Table III. Note that dispersion of LPP mode 8 is very small and within B_u $\omega_{\mathrm{TO},6}$ and $\omega_{\mathrm{TO},7}$.

nanoribbons by infrared reflectance spectroscopy [94] but no quantitative model analysis of the reflectance spectra was provided.

LPP modes. The LPP modes with A_u and B_u symmetry follow from Eqs. (26) and (25), respectively. The general

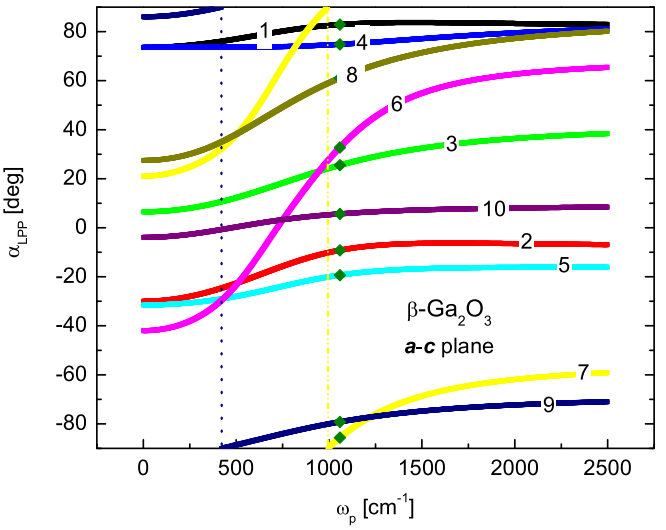

FIG. 13. Unit eigendisplacement vectors of the LPP coupled modes polarized within the **a**-**c** plane as a function of isotropic plasma frequency ω_p. Note that the free plasma like modes 1 and 2 approach **x** and **y** in Fig. 2 for $\omega_p \to \infty$. Symbols (diamonds) indicate vectors derived for the samples studied in this work. Numbering of modes as shown in Table III.

TABLE III. LPP frequency parameters for A_u and B_u modes obtained from best match model analysis of $\varepsilon_{xx},\varepsilon_{yy},\varepsilon_{zz}$, and ε_{xy}. Also given are the eigenvector polarization angles α_{LPP} relative to **c**. The last digit which is determined within the 90% confidence interval is indicated with parentheses.

Parameter	$k=1$	2	3	4	5	6	7	8	9	10
$\omega_{\mathrm{LPP},k}$ (cm^{-1}) (B_u)	967.(1)	872.(9)	730.(7)	638.(2)	458.(1)	357.(9)	331.(8)	277.(4)	226.(4)	188.(8)
$\alpha_{\mathrm{LPP},k}$ (deg) (B_u)	179.(3)	91.(1)	35.(4)	76.(8)	160.(8)	36.(7)	91.(7)	67.(4)	100.(8)	6.(7)
$\omega_{\mathrm{LPP},k}$ (cm^{-1}) (A_u)	88(5)	60(3)	38(0)	23(9)	15(4)					

solutions of these equations provide 5 LPP modes with A_u, and 10 LPP modes with B_u symmetry. We found an isotropic plasma frequency parameter of $\omega_{\mathrm{p},x}=\omega_{\mathrm{p},y}=\omega_{\mathrm{p},z}=\omega_{\mathrm{p}}=1058.3$ cm^{-1} sufficient to match all spectra $\varepsilon_{xx},\varepsilon_{yy}$, and ε_{zz} (Table IV). This value is used to derive the LPP modes for our samples. We further assume that all samples investigated here share the same set of free charge carriers. This assumption is reasonable since both specimens were cut from the same bulk crystal. However, small gradients in Sn dopant volume density may exist throughout the bulk crystal due to the directional growth method and diffusion gradients near the solution solid interface [90,92]. The resulting LPP mode frequencies are then summarized in Table III.

LPP mode dispersion. The LPP mode coupling for A_u symmetry is trivial and equivalent to any other semiconductor material whose unit eigendisplacement vectors are all parallel and/or orthogonal. Coupling for modes with B_u symmetry is not trivial. Equation (25) describes the LO plasmon coupling, and predicts the LPP mode frequencies within a given sample as a function of the free charge carrier properties. For β-Ga_2O_3, the effective mass parameter anisotropy may need to be considered. Presently, available information suggests that the effective mass is nearly isotropic (see below). We therefore choose to render the effects of free charge carriers by using an isotropic plasma frequency contribution, ω_{p}. We plot the resulting LPP modes with B_u symmetry in Fig. 12 as a function of ω_{p}. We also plot their unit eigendisplacement vectors obtained from Eq. (27) in Fig. 13.

A mode-branch-like behavior with phonon-like and plasma-like branches similar to orthogonal eigenvector lattice materials can be seen. For $\omega_p \to 0$, the upper LPP branches emerge from LO mode frequencies, and the lowest 2 branches behave like uncoupled plasma modes. For $\omega_p \to \infty$, the 2 upper LPP branches behave like uncoupled plasma modes, and the lower branches behave like TO modes. Each LPP mode merges with one TO mode except for 2 high-frequency plasma-like branches. The unit eigendisplacement vectors of the 2 plasma-like modes approach the x and y directions for large plasma frequencies, and indicate a quasiorthorhombic free charge carrier response towards visible light optical frequencies. For intermediate ω_p, the LPP coupling causes branch crossing with TO modes, which do not occur in orthogonal eigenvector lattice materials. The horizontal lines in Fig. 12 indicate the B_u symmetry TO modes.

Free charge carrier properties. Table IV summarizes the Drude model parameters obtained from $\varepsilon_{xx},\varepsilon_{yy}$, and ε_{zz}. For ε_{xy} no significant Drude contribution was detected. In order to derive the free charge carrier density and mobility parameters from the plasma frequency and broadening parameters one needs the effective mass parameters. Unless magnetic fields are exploited and the optical Hall effect can be measured [93,95–101], long-wavelength ellipsometry requires these parameters from auxiliary investigations.

Experimental data on the electron effective mass in β-Ga_2O_3 are not exhaustive. Early estimates suggested 0.55 m_e [8]. A recent calculation predicts the effective electron mass at the Γ point of the Brillouin zone almost isotropic with values between 0.27 m_e and 0.28 m_e, depending on direction [29]. These values agree with experimental measurements from angular-resolved photoemission spectroscopy (ARPES) on a $\mathbf{b}^\star\mathbf{c}^\star$-cleavage plane of (100) β-Ga_2O_3 (0.28 m_e; Ref. [32,33]). Earlier calculations using various approaches obtained 0.28 m_e [102,103], 0.34m_e [25], and 0.390m_e [7]. Calculations that did not use a hybrid functional approach led to smaller values of (0.23 . . . 0.24) m_e in the local density approximation [30] and (0.12 . . . 0.13) m_e in the generalized gradient approximation [31]. He *et al.* reported slightly anisotropic electron effective mass values with $m_{\mathbf{a}^\star}=0.123\ m_e$, $m_{\mathbf{c}^\star}=0.124\ m_e$, and $m_{\mathbf{b}^\star}=0.130\ m_e$, along axes $\mathbf{a}^\star$,$\mathbf{c}^\star$, and $\mathbf{b}^\star$, respectively, with ratios $m_{\mathbf{a}^\star}/m_{\mathbf{c}^\star}=0.99$ and $m_{\mathbf{b}^\star}/m_{\mathbf{c}^\star}=1.05$ [31]. Yamaguchi also reported values with small anisotropy $m_{xx}=0.2315\ m_e$, $m_{yy}=0.2418\ m_e$, and $m_{zz}=0.2270\ m_e$ using a first-principles full-potential linearized augmented plane wave method [30]. For analysis of the FIR-GSE and IR-GSE data we

TABLE IV. Best match model parameters for free charge carrier contributions, static, and high-frequency dielectric constants. From our analysis we also obtain $\varepsilon_{\mathrm{DC},xy}=-0.1(3)$ and $\varepsilon_{\infty,xy}=-0.0(8)$ consistent with the generalized LST relation in Eq. (29). Values reported from our analysis for $\varepsilon_{\mathrm{DC},zz}$ and $\varepsilon_{\infty,zz}$ are consistent with the traditional LST relation in Eq. (28) with TO and LO modes given in Table II.

		ε_{xx} (**a**)	ε_{yy} ($\mathbf{c}^\star$)	ε_{zz}(**b**)
$\gamma_{\mathrm{p},(j)}$ (cm^{-1})	This work	37(0)	69(6)	36(1)
$\mu_{(j)}$ [cm^2/(V s)]	This work	9(0)	4(8)	9(2)
$\varepsilon_{\infty,(j)}$	This work	3.7(5)	3.2(1)	3.7(1)
$\varepsilon_{\mathrm{DC},(j)}$	This work	12.(7)	10.(9)	11.(2)
$\varepsilon_{\infty,(j)}$	Theory Ref. [28]	3.81[a]	3.85[a]	4.08[a]
$\varepsilon_{\mathrm{DC},(j)}$	Theory Ref. [28]	10.84[a]	13.89[a]	11.49[a]
$\varepsilon_{\infty,(j)}$	Theory Ref. [25]	2.86[a]	2.78[a]	2.84[a]
ε_∞	Expt. Ref. [27]		3.57[b]	
ε_∞	Expt. Ref. [22]		3.53[b]	
$\varepsilon_{\mathrm{DC}}$	Expt. Ref. [23]		9.9–10.2[b]	
$\varepsilon_{\mathrm{DC}}$	Expt. Ref. [24]		10.2[b]	
ε_∞	Expt. Ref. [26]		3.6[b]	
$\varepsilon_{\mathrm{DC}}$	Expt. Ref. [26]		9.57[b]	

[a]Crystal axes assignment unknown.
[b]Isotropic average from films.

assume an isotropic effective electron mass value of 0.28 m_e, which appears to be a good compromise of the experimental and theoretical data. We then obtain $N = 3.(5) \times 10^{18}$ cm^{-3} and anisotropic mobility parameters given in Table IV. We observe similar mobility values along axes **a** and **b** and an about 2 times smaller mobility value perpendicular to **a** and **b**.

Static and high-frequency dielectric constant. Table IV also summarizes static and high-frequency dielectric constants obtained in this work. We observe no significant contributions, with $\varepsilon_{\mathrm{DC},xy} = -0.13$ and $\varepsilon_{\infty,xy} = -0.08$ for $\omega \to 0$ and $\omega \to \infty$, respectively. At DC frequencies, β-Ga_2O_3 behaves quasiorthorhombically. We find that $\varepsilon_{\mathrm{DC},xx}$ (12.7) > $\varepsilon_{\mathrm{DC},zz}$ (11.2) > $\varepsilon_{\mathrm{DC},yy}$ (10.9), predicting anisotropy at DC frequencies. In the high-frequency limit, which is merely above the reststrahlen range for this work, β-Ga_2O_3 behaves nearly as an optically uniaxial crystal, with $\varepsilon_{\mathrm{DC},xx}$ (3.75) ≈ $\varepsilon_{\mathrm{DC},zz}$ (3.71) > $\varepsilon_{\mathrm{DC},yy}$ (3.21). Data for the x-y (**a**-**c**) plane are consistent with the generalized LST relation in Eq. (29), and for axis **b** with Eq. (28). An isotropic average between all values obtained here is $\varepsilon_{\mathrm{DC}} = 11.6$ and $\varepsilon_{\infty} = 3.56$. A static dielectric constant between 9.9 and 10.2 was measured on films deposited by electron beam evaporation and annealing onto silicon and GaAs [22], and 10.2 was measured for single-crystal β-Ga_2O_3 platelets in the direction perpendicular to the (100) plane at radio frequencies (5 kHz to 500 kHz) [24]. Schmitz, Gassmann, and Franchy report static and high-frequency values from line shape analysis of electron energy loss spectroscopy data from β-Ga_2O_3 films on metal substrates [26]. Values obtained previously for films agree well with our isotropic average [22,26,27], while previously reported isotropic DC values are slightly smaller [23,24,26]. Data from recent band structure calculations are included in Table IV and show some agreement with our results [25,28]. Because it appears that our present work is the first comprehensive analysis of the long-wavelength dielectric function tensor of single-crystal β-Ga_2O_3 we believe that our data likely represent so far the most accurate values for this monoclinic semiconductor. Finally, the effective monoclinic angles near DC and high frequencies (above the reststrahlen range), according to Eqs. (14) and (16), respectively, approach 90° because $\varepsilon_{xy} \approx 0$, both at $\omega \to 0$ and $\omega \to \infty$.

C. Mode nonharmonicity

In Eq. (10) we implemented simple, Lorentzian-broadened harmonic oscillator functions to account for the dielectric polarizability of the individual TO resonances. With these functions we obtained nearly perfect match between the point-by-point extracted dielectric tensor elements and our best-match model parameters. In Figs. 7–10 both data sets are nearly indistinguishable. However, subtle discrepancies remain between the two data sets. Figure 14 shows the real and imaginary parts of the function $\varepsilon_{xx}\varepsilon_{yy} - \varepsilon_{xy}^2$, and the negated imaginary part of the inverse of ε_{zz} using the same data sets shown in Figs. 7–10. The inverse of the dielectric function conveniently reflects the spectral location of the LPP modes, which produce maxima in the imaginary part of the dielectric loss function. However, as can be seen in the lower panel of Fig. 14, the agreement is less obvious for axis **b**. The cause for this disagreement is likely given in the fact

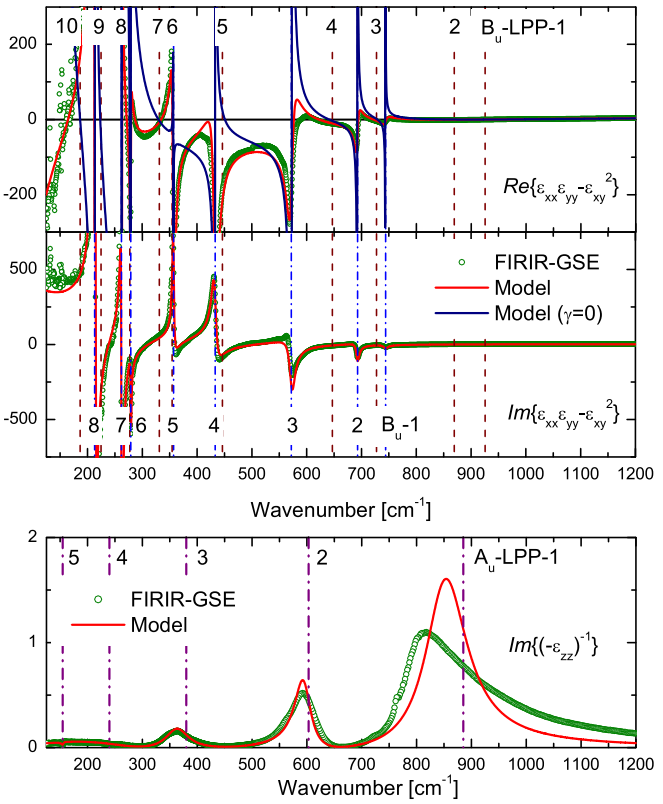

FIG. 14. Top panels: Real and imaginary parts of function $\varepsilon_{xx}\varepsilon_{yy} - \varepsilon_{xy}^2$. Vertical lines indicate B_u mode TO (dashed lines) and LPP frequencies (dash dotted lines). Bottom panel: Imaginary part of $-\varepsilon_{zz}^{-1}$. Vertical lines indicate A_u mode LPP frequencies.

that nonharmonic broadening effects were not considered in this work. It is well known that the harmonic oscillator model fails to correctly describe the long-wavelength response near LO frequencies in crystals with multiple polar phonon modes. It was pointed out and demonstrated by Gervais and coworkers that interactions between normal vibration modes by nonharmonic coupling give raise to nonharmonic dielectric response behavior [104–107]. The phonon mode energies of crystals with a large number of phonon branches suffer a complex self-energy shift, which can be both frequency and temperature dependent. Gervais and Piriou introduced a simple, so called four-parameter semiquantum (FPSQ) function to correctly model long-wavelength reflectance of multiple phonon mode crystals [105,106]. This model suggests independent broadening parameters for each LO and TO lattice mode. Gervais and Piriou used this factorized form to calculate the ordinary dielectric functions from IR-reflectivity data of c-plane α-Al_2O_3, rutile TiO_2, and α-SiO_2. We recently used this model to obtain highly accurate infrared dielectric model functions for anisotropic materials such as corundum [52], rutile [55], and antimonite [56]. Similar discrepancies due to the same subtle differences can be seen between the point-by-point data set and best-model calculated functions $\varepsilon_{xx}\varepsilon_{yy} - \varepsilon_{xy}^2$ in Fig. 14. Also shown is the best-model calculated function $\varepsilon_{xx}\varepsilon_{yy} - \varepsilon_{xy}^2$ by setting all broadening parameters to zero. The zero-broadening function fully envelopes the point-by-point data and best-match model data. It is obvious that function

$\varepsilon_{xx}\varepsilon_{yy} - \varepsilon_{xy}^2$ is governed by the poles and zeros given by the B_u symmetry TO and LPP modes, respectively. It can be further seen that the poles are clearly rendered by the spectral behavior of the point-by-point data while the LPP modes must be obtained by a numerical root finding procedure on the zero-broadening model function. Because the harmonic oscillator model functions do not precisely match the point-by-point data in the spectral regions of the LPP modes, one must anticipate that the thereby obtained LPP (LO) modes carry larger uncertainty than the TO modes. Future work must seek better model descriptions to account for the nonharmonic broadening, for example by allowing for coupling between the individual eigenresonances in Eq. (2). Importantly, for accurate analysis of free charge carrier properties from long-wavelength investigations of simple or complex layer structures, accurate description of the nonharmonic lattice and free charge carrier mode coupling in monoclinic semiconductors is a prerequisite. In the same vein, model parameters for static and high-frequency behavior must be considered with care. At present, these parameters may subsume small offsets not provided by the oscillator functions currently used upon the best-match calculation procedure. Also, experimental data near the DC region or near the visible spectral region have not yet been included in the GSE analysis. Investigations at THz frequencies as well as within the near-infrared spectral region may provide more accurate results. Nonetheless, we believe that parameters reported here for LO and LPP modes as well as for the model dielectric function tensor components may serve as a good starting point for further work.

V. CONCLUSIONS

A dielectric function tensor model approach suitable for calculating the optical response of monoclinic and triclinic symmetry materials with multiple uncoupled long-wavelength active modes was presented. The approach was applied to monoclinic β-Ga_2O_3 single-crystal samples. Surfaces cut under different angles from a bulk crystal, (010) and $(\bar{2}01)$, are investigated by generalized spectroscopic ellipsometry within infrared and far-infrared spectral regions. We determined the frequency dependence of 4 independent β-Ga_2O_3 Cartesian dielectric function tensor elements by matching large sets of experimental data using a polyfit, wavelength-by-wavelength data inversion approach. From matching our monoclinic model to the obtained 4 dielectric function tensor components, we determined 4 pairs of transverse and longitudinal optic phonon modes with A_u symmetry, and 8 pairs with B_u symmetry, and their eigenvectors within the monoclinic lattice. We observe that the TO-LO rule is broken for modes with B_u symmetry. We further report on density functional theory calculations on the infrared and far-infrared optical phonon modes, which are in excellent agreement with our experimental findings. We derived and reported density and anisotropic mobility parameters of the free charge carriers within the tin-doped crystals. We observed 5 longitudinal phonon plasmon coupled modes in β-Ga_2O_3 with A_u symmetry and 10 modes with B_u symmetry. We discussed and presented their dependence on an isotropic free charge carrier plasma. We also discussed and presented monoclinic dielectric constants for static electric fields and frequencies above the reststrahlen range, and we provided a generalization of the Lyddane-Sachs-Teller relation for monoclinic lattices with infrared and far-infrared active modes. We observed that the generalized Lyddane-Sachs-Teller relation is fulfilled excellently for β-Ga_2O_3. The model provided in this work will establish a useful base for infrared and far-infrared ellipsometry analysis of homo- and heteroepitaxial layers grown on arbitrary faces of β-Ga_2O_3 substrates.

ACKNOWLEDGMENTS

This work was supported in part by the National Science Foundation (NSF) through the Center for Nanohybrid Functional Materials (EPS-1004094), the Nebraska Materials Research Science and Engineering Center (DMR-1420645), and awards CMMI 1337856 and EAR 1521428. We acknowledge further support from the Swedish Research Council (VR) under Grants No. 2013-5580 and No. 2010-3848, the Swedish Governmental Agency for Innovation Systems (VINNOVA) under the VINNMER international qualification program, Grants No. 2011-03486 and No. 2014-04712, and the Swedish Foundation for Strategic Research (SSF) under Grants No. FFL12-0181 and No. RIF14-055. The financial support by the Linköping Linnaeus Initiative on Nanoscale Functional Materials (LiLiNFM) supported by VR is gratefully acknowledged. The authors further acknowledge grant support by the University of Nebraska–Lincoln, the J. A. Woollam Co., Inc., and the J. A. Woollam Foundation. DFT calculations were performed using the resources of the Holland Computing Center at the University of Nebraska–Lincoln.

[1] C. G. Granqvist, *Handbook of Inorganic Electrochromic Materials* (Elsevier, Amsterdam, 1995).
[2] D. Gogova, A. Iossifova, T. Ivanova, Z. Dimitrova, and K. Gesheva, J. Cryst. Growth **198-199**, 1230 (1999).
[3] U. Betz, M. K. Olsson, J. Marthy, M. F. Escola, and F. Atamny, Surf. Coat. Technol. **200**, 5751 (2006).
[4] F. Reti, M. Fleischer, H. Meixner, and J. Giber, Sens. Act. B **19**, 573 (1994).
[5] R. Roy, V. G. Hill, and E. F. Osborn, J. Am. Chem. Soc. **74**, 719 (1952).
[6] H. H. Tippins, Phys. Rev. **140**, A316 (1965).
[7] M.-G. Ju, X. Wang, W. Liang, Y. Zhao, and C. Li, J. Mater. Chem. A **2**, 17005 (2014).
[8] N. Ueda, H. Hosono, R. Waseda, and H. Kawazoe, Appl. Phys. Lett. **70**, 3561 (1997).
[9] J. Wager, Science **300**, 1245 (2003).
[10] K. Sasaki, M. Higashiwaki, A. Kuramata, T. Masui, and S. Yamakoshi, J. Cryst. Growth **378**, 591 (2013).
[11] B. J. Baliga, IEEE Electron. Dev. Lett. **10**, 455 (1989).

[12] Y. Tomm, P. Reiche, D. Klimm, and T. Fukuda, J. Cryst. Growth **220**, 510 (2000).

[13] E. G. Villora, K. Shimamura, Y. Yoshikawa, K. Aoki, and N. Ichinose, J. Cryst. Growth **270**, 420 (2004).

[14] M. Higashiwaki, K. Sasaki, A. Kuramata, T. Masui, and S. Yamakoshi, Phys. Status Solidi A **211**, 21 (2014).

[15] D. Gogova, P. P. Petrov, M. Buegler, M. R. Wagner, C. Nenstiel, G. Callsen, M. Schmidbauer, R. Kucharski, M. Zajac, R. Dwilinski *et al.*, J. Appl. Phys. **113**, 203513 (2013).

[16] D. Gogova, M. Schmidbauer, and A. Kwasniewski, CrystEngComm **17**, 6744 (2015).

[17] E. Betzig, J. K. Trautman, T. D. Harris, J. S. Weiner, and R. L. Kostelak, Science **251**, 1468 (1991).

[18] M. Oto, S. Kikugawa, N. Sarukura, M. Hirano, and H. Hosono, IEEE Photonics Technol. Lett. **13**, 978 (2001).

[19] A. Shionoya and W. M. Yen, *Phosphor Handbook* (CRC Press, Boca Raton, FL, 1998).

[20] T. Miyata, T. Nakatani, and T. Minami, J. Luminesc. **87-89**, 1183 (2000).

[21] E. G. Villora, Y. Morioka, T. Atou, T. Sugawara, M. Kikuchi, and T. Fukuda, Phys. Status Solidi A **193**, 187195 (2002).

[22] M. Passlack, E. F. Schubert, W. S. Hobson, M. Hong, N. Moriya, S. N. G. Chu, K. Konstadinidis, J. P. Mannaerts, M. L. Schnoes, and G. J. Zydzik, J. Appl. Phys. **77**, 686 (1995).

[23] M. Passlack, N. E. J. Hunt, E. F. Schubert, G. J. Zydzik, M. Hong, J. P. Mannaerts, R. L. Opila, and R. J. Fischer, Appl. Phys. Lett. **64**, 2715 (1994).

[24] B. Hoeneisen, C. A. Mead, and M.-A. Nicolet, Solid State Electronics **14**, 1057 (1971).

[25] H. He, R. Orlando, M. A. Blanco, R. Pandey, E. Amzallag, I. Baraille, and M. Rerat, Phys. Rev. B **74**, 195123 (2006).

[26] G. Schmitz, P. Gassmann, and R. Franchy, J. Appl. Phys. **83**, 2533 (1998).

[27] M. Rebien, W. Henrion, M. Hong, J. P. Mannaerts, and M. Fleischer, Appl. Phys. Lett. **81**, 250 (2002).

[28] B. Liu, M. Gu, and X. Liu, App. Phys. Lett. **91**, 172102 (2007).

[29] H. Peelaers and C. G. V. de Walle, Phys. Status Solidi B **252**, 828 (2015).

[30] K. Yamaguchi, Solid State Commun. **131**, 739 (2004).

[31] H. He, M. A. Blanco, and R. Pandey, Appl. Phys. Lett. **88**, 261904 (2006).

[32] M. Mohamed, C. Janowitz, I. Unger, R. Manzke, Z. Galazka, R. Uecker, R. Fornari, J. R. Weber, J. B. Varley, and C. G. V. de Walle, Appl. Phys. Lett. **97**, 211903 (2010).

[33] C. Janowitz, V. Scherer, M. Mohamed, A. Krapf, H. Dwelk, R. Manzke, Z. Galazka, R. Uecker, K. Irmscher, and R. Fornari, New J. Phys. **13**, 085014 (2011).

[34] Z. Guo, A. Verma, X. Wu, F. Sun, A. Hickman, T. Masui, A. Kuramata, M. Higashiwaki, D. Jena, and T. Luo, Appl. Phys. Lett. **106**, 111909 (2015).

[35] P. Drude, Ann. Phys. **268**, 584 (1887).

[36] P. Drude, Ann. Phys. **270**, 489 (1888).

[37] P. Drude, *Lehrbuch der Optik* (S. Hirzel, Leipzig, 1900) (English translation by Longmans, Green, and Company, London, 1902; reissued by Dover, New York, 2005).

[38] M. Schubert, Ann. Phys. **15**, 480 (2006).

[39] G. E. Jellison, M. A. McGuire, L. A. Boatner, J. D. Budai, E. D. Specht, and D. J. Singh, Phys. Rev. B **84**, 195439 (2011).

[40] A. B. Kuzmenko, D. van der Marel, P. J. M. van Bentum, E. A. Tishchenko, C. Presura, and A. A. Bush, Phys. Rev. B **63**, 094303 (2001).

[41] T. Möller, P. Becker, L. Bohatý, J. Hemberger, and M. Grüninger, Phys. Rev. B **90**, 155105 (2014).

[42] M. Born and K. Huang, *Dynamical Theory of Crystal Lattices* (Clarendon, Oxford, 1954).

[43] A. B. Kuz'menko, E. A. Tishchenko, and V. G. Orlov, J Phys.: Condens. Matter **8**, 6199 (1996).

[44] S. Geller, J. Chem. Phys. **33**, 676 (1960).

[45] M. Dressel and G. Grüner, *Electrodynamics of Solids* (Cambridge University Press, Cambridge, 2002).

[46] J. D. Jackson, *Classical Electrodynamics* (J. Wiley & Sons, New York, 1975).

[47] M. Schubert, *Infrared Ellipsometry on Semiconductor Layer Structures: Phonons, Plasmons, and Polaritons*, Vol. 209 of Springer Tracts in Modern Physics (Springer, Berlin, 2004).

[48] J. Humlíček and T. Zettler, in *Handbook of Ellipsometry*, edited by E. A. Irene and H. W. Tompkins (William Andrew Publishing, Norwich, 2004).

[49] C. Kittel, *Introduction to Solid States Physics* (Wiley, Hoboken, 2005).

[50] H. Fujiwara, *Spectroscopic Ellipsometry* (John Wiley & Sons, New York, 2007).

[51] C. Pidgeon, in *Handbook on Semiconductors*, edited by M. Balkanski (North-Holland, Amsterdam, 1980).

[52] M. Schubert, T. E. Tiwald, and C. M. Herzinger, Phys. Rev. B **61**, 8187 (2000).

[53] R. H. Lyddane, R. Sachs, and E. Teller, Phys. Rev. **59**, 673 (1941).

[54] W. Cochran and R. A. Cowley, J. Phys. Chem. Solids **23**, 447 (1962).

[55] S. Schöche, T. Hofmann, R. Korlacki, T. E. Tiwald, and M. Schubert, J. Appl. Phys. **113**, 164102 (2013).

[56] M. Schubert, T. Hofmann, C. M. Herzinger, and W. Dollase, Thin Solid Films **455-456**, 619 (2004).

[57] M. Dressel, B. Gompf, D. Faltermeier, A. K. Tripathi, J. Pflaum, and M. Schubert, Opt. Exp. **16**, 19770 (2008).

[58] M. Schubert, C. Bundesmann, G. Jakopic, and H. Arwin, Appl. Phys. Lett. **84**, 200 (2004).

[59] N. Ashkenov, B. N. Mbenkum, C. Bundesmann, V. Riede, M. Lorenz, E. M. Kaidashev, A. Kasic, M. Schubert, M. Grundmann, G. Wagner *et al.*, J. Appl. Phys. **93**, 126 (2003).

[60] A. Kasic, M. Schubert, S. Einfeldt, D. Hommel, and T. E. Tiwald, Phys. Rev. B **62**, 7365 (2000).

[61] A. Kasic, M. Schubert, Y. Saito, Y. Nanishi, and G. Wagner, Phys. Rev. B **65**, 115206 (2002).

[62] V. Darakchieva, P. P. Paskov, E. Valcheva, T. Paskova, B. Monemar, M. Schubert, H. Lu, and W. J. Schaff, Appl. Phys. Lett. **84**, 3636 (2004).

[63] V. Darakchieva, J. Birch, M. Schubert, T. Paskova, S. Tungasmita, G. Wagner, A. Kasic, and B. Monemar, Phys. Rev. B **70**, 045411 (2004).

[64] V. Darakchieva, E. Valcheva, P. P. Paskov, M. Schubert, T. Paskova, B. Monemar, H. Amano, and I. Akasaki, Phys. Rev. B **71**, 115329 (2005).

[65] V. Darakchieva, T. Paskova, M. Schubert, H. Arwin, P. P. Paskov, B. Monemar, D. Hommel, M. Heuken, J. Off, F. Scholz *et al.*, Phys. Rev. B **75**, 195217 (2007).

[66] V. Darakchieva, M. Schubert, T. Hofmann, B. Monemar, Y. Takagi, and Y. Nanishi, Appl. Phys. Lett. **95**, 202103 (2009).

[67] V. Darakchieva, T. Hofmann, M. Schubert, B. E. Sernelius, B. Monemar, P. O. A. Persson, F. Giuliani, E. Alves, H. Lu, and W. J. Schaff, Appl. Phys. Lett. **94**, 022109 (2009).

[68] V. Darakchieva, K. Lorenz, N. Barradas, E. Alves, B. Monemar, M. Schubert, N. Franco, C. Hsiao, L. Chen, W. Schaff *et al.*, Appl. Phys. Lett. **96**, 081907 (2010).

[69] M.-Y. Xie, M. Schubert, J. Lu, P. O. A. Persson, V. Stanishev, C. L. Hsiao, L. C. Chen, W. J. Schaff, and V. Darakchieva, Phys. Rev. B **90**, 195306 (2014).

[70] M.-Y. Xie, N. B. Sedrine, S. Schöche, T. Hofmann, M. Schubert, L. Hong, B. Monemar, X. Wang, A. Yoshikawa, K. Wang *et al.*, J. Appl. Phys. **115**, 163504 (2014).

[71] T. Hofmann, D. Schmidt, and M. Schubert, *Ellipsometry at the Nanoscale* (Springer, Berlin, 2013), pp. 411–428.

[72] C. Bundesmann, N. Ashkenov, M. Schubert, A. Rahm, H. v. Wenckstern, E. M. Kaidashev, M. Lorenz, and M. Grundmann, Thin Solid Films **455-456**, 161 (2004).

[73] V. Darakchieva, T. Paskova, P. P. Paskov, H. Arwin, M. Schubert, B. Monemar, S. Figge, D. Hommel, B. A. Haskell, P. T. Fini *et al.*, Phys. Status Solidi B **243**, 1594 (2006).

[74] V. Darakehieva, T. Paskova, M. Schubert, P. P. Paskov, H. Arwin, B. Monemar, D. Hommel, M. Heuken, J. Off, B. A. Haskell *et al.*, J. Cryst. Growth **300**, 233 (2007).

[75] V. Darakchieva, T. Paskova, and M. Schubert, *Group-III Nitrides with Nonpolar Surfaces: Growth, Properties, and Devices* (Wiley, Berlin, 2008), pp. 219–253.

[76] H. Thompkins and E. A. Irene, editors, *Handbook of Ellipsometry* (William Andrew Publishing, Highland Mills, 2004).

[77] R. M. A. Azzam, in *Handbook of Optics* (McGraw-Hill, New York, 1995), Vol. 2, Chap. 27, 2nd ed.

[78] G. E. Jellison, in *Handbook of Ellipsometry*, edited by E. A. Irene and H. W. Tompkins (William Andrew Publishing, Norwich, 2004).

[79] D. E. Aspnes, in *Handbook of Optical Constants of Solids*, edited by E. Palik (Academic, New York, 1998).

[80] M. Schubert, Phys. Rev. B **53**, 4265 (1996).

[81] M. Schubert, in *Introduction to Complex Mediums for Optics and Electromagnetics*, edited by W. S. Weiglhofer and A. Lakhtakia (SPIE, Bellingham, 2003).

[82] M. Schubert, in *Handbook of Ellipsometry*, edited by E. Irene and H. Tompkins (William Andrew Publishing, Norwich, 2004).

[83] T. Hofmann, V. Gottschalch, and M. Schubert, Phys. Rev. B **66**, 195204 (2002).

[84] P. Giannozzi, S. Baroni, N. Bonini, M. Calandra, R. Car, C. Cavazzoni, D. Ceresoli, G. L. Chiarotti, M. Cococcioni, I. Dabo *et al.*, J. Phys.: Condens. Matter **21**, 395502 (2009).

[85] J. P. Perdew and A. Zunger, Phys. Rev. B **23**, 5048 (1981).

[86] H. J. Monkhorst and J. D. Pack, Phys. Rev. B **13**, 5188 (1976).

[87] S. Baroni, S. de Gironcoli, A. D. Corso, S. Baroni, S. de Gironcoli, and P. Giannozzi, Rev. Mod. Phys. **73**, 515 (2001).

[88] A. Kokalj, Comput. Mater. Sci. **28**, 155 (2003).

[89] URL http://www.xcrysden.org/.

[90] H. Aida, K. Nishiguchi, H. Takeda, N. Aota, K. Sunakawa, and Y. Yaguchi, Jpn. J. Appl. Phys. **47**, 8506 (2008).

[91] K. Sasaki, A. Kuramata, T. Masui, E. G. Villora, K. Shimamura, and S. Yamakoshi, Appl. Phys. Exp. **5**, 035502 (2012).

[92] K. Shimamura and E. G. Villora, Act. Phys. Pol. A **124**, 265 (2013).

[93] P. Kühne, C. M. Herzinger, M. Schubert, J. A. Woollam, and T. Hofmann, Rev. Sci. Instrum. **85**, 071301 (2014).

[94] V. M. Bermudez and S. M. Prokes, Langmuir **23**, 12566 (2007).

[95] M. Schubert, T. Hofmann, and C. M. Herzinger, J. Opt. Soc. Am. A **20**, 347 (2003).

[96] T. Hofmann, U. Schade, K. C. Agarwal, B. Daniel, C. Klingshirn, M. Hetterich, C. M. Herzinger, and M. Schubert, Appl. Phys. Lett. **88**, 042105 (2006).

[97] T. Hofmann, M. Schubert, G. Leibiger, and V. Gottschalch, Appl. Phys. Lett. **90**, 182110 (2007).

[98] T. Hofmann, V. Darakchieva, B. Monemar, H. Lu, W. Schaff, and M. Schubert, J. Electron. Mater. **37**, 611 (2008).

[99] S. Schöche, J. Shi, A. Boosalis, P. Kühne, C. M. Herzinger, J. A. Woollam, W. J. Schaff, L. F. Eastman, M. Schubert, and T. Hofmann, Appl. Phys. Lett. **98**, 092103 (2011).

[100] P. Kühne, V. Darakchieva, R. Yakimova, J. D. Tedesco, R. L. Myers-Ward, C. R. Eddy, D. K. Gaskill, C. M. Herzinger, J. A. Woollam, M. Schubert *et al.*, Phys. Rev. Lett. **111**, 077402 (2013).

[101] S. Schöche, P. Kühne, T. Hofmann, M. Schubert, D. Nilsson, A. Kakanakova-Georgieva, E. Janzén, and V. Darakchieva, Appl. Phys. Lett. **103**, 212107 (2013).

[102] J. B. Varley, J. R. Weber, A. Janotti, and C. G. V. de Walle, Appl. Phys. Lett. **97**, 142106 (2010).

[103] W. S. Hwang, A. Verma, H. Peelaers, V. Protasenko, S. Rouvimov, H. G. Xing, A. Seabaugh, W. Haensch, C. V. de Walle, Z. Galazka *et al.*, Appl. Phys. Lett. **104**, 203111 (2014).

[104] F. Gervais, Solid State Commun. **13**, 1211 (1973).

[105] F. Gervais and B. Piriou, J. Phys. C: Solid State Phys. **7**, 2374 (1974).

[106] F. Gervais and B. Piriou, Phys. Rev. B **11**, 3944 (1975).

[107] F. Gervais, in *Handbook of Optical Constants of Solids*, edited by E. D. Palik (Academic Press, Orlando, 1985), Vol. 1, p. 177.